NEHRP AWARD 07HQGR0108

USGS Final Technical Report

Placing Bounds on the endpoints and Surface-Slip distribution characteristics of future surface rupture earthquakes.

Steven G. Wesnousky
Center for Neotectonic Studies
University of Nevada, Reno
1664 North Virginia Avenue
Reno, Nevada 89557
775-784-6067 (tel)
wesnousky@unr.edu
http://neotectonics.seismo.unr.edu

Bulletin of the Seismological Society of America, Vol. 98, No. 4, pp. 1609–1632, August 2008, doi: 10.1785/0120070111

Ⓔ

Displacement and Geometrical Characteristics of Earthquake Surface Ruptures: Issues and Implications for Seismic-Hazard Analysis and the Process of Earthquake Rupture

by Steven G. Wesnousky

Abstract There now exist about three dozen historical earthquakes for which investigators have constructed maps of earthquake rupture traces accompanied by descriptions of the coseismic slip observed along the fault strike. The maps and slip distributions are compiled here to place observational bounds on aspects of seismic-hazard analysis and fault mechanics. Analysis leads to an initial statistical basis to predict the end points of rupture and the amount of surface slip expected at sites along the strike during earthquakes on mapped faults. The observations also give support to the ideas that there exists a process zone or volume of about 3–4 km in dimension at the fronts of large laterally propagating earthquake ruptures within which stress changes may be sufficient to trigger slip on adjacent faults, and that the ultimate length of earthquake ruptures is controlled primarily by the geometrical complexity of fault traces and variations in accumulated stress levels along faults that arise due to the location of past earthquakes. To this may be added the observation that the form of earthquake surface-slip distributions is better described by asymmetric rather than symmetric curve forms and that earthquake epicenters do not appear to correlate in any systematic manner to regions of maximum surface slip observed along strike.

Online Material: Maps of surface ruptures, digitized values and curve fits to surface-slip distributions, and notes and references for Tables 1 and 2.

Introduction

It has become standard practice since Clark's (1972) early study of the 1968 Borrego Mountain earthquake to map the geometry of rupture traces and assess the surface-slip distribution of large earthquakes that break the ground surface. The results of such studies have been a steady source of reference in development of seismic hazard methodologies (e.g., Wesnousky *et al.*, 1984; Wesnousky, 1986; Petersen and Wesnousky, 1994; Working Group on California Earthquake Probabilities [WGCEP], 1995; Frankel and Petersen, 2002), engineering design criteria for critical facilities (e.g., Kramer, 1996; Pezzopane and Dawson, 1996; Fuis and Wald, 2003), and development and discussion of mechanical models to understand physical factors that control the dynamics of the earthquake source as well as the resulting strong ground motions (e.g., Scholz, 1982a; Scholz, 1982b; Heaton, 1990; Romanowicz, 1994; Scholz, 1994; Bodin and Brune, 1996; King and Wesnousky, 2007). There now exist about three dozen historical earthquakes for which investigators have constructed maps of earthquake rupture traces accompanied by data describing the coseismic slip observed along the fault strike. Here, I put forth a compilation of that data set with the aim of placing observational bounds on aspects of seismic-hazard analysis and fault mechanics.

Data Set

I limit my attention to the larger surface rupture earthquakes of length dimension greater than about 15 km and for which there exist both maps and measurements of coseismic offset along the strike of the rupture (Table 1). The map and slip distributions of the 9 April 1968 M_w 6.1 Borrego Mountain earthquake of California illustrate the manner of data compilation (Fig. 1). The surface-slip distribution is placed below the map of the surface rupture trace and each is drawn to the same distance scale. Nearby fault traces that displace Quaternary and younger deposits but did not rupture during the earthquake are also shown. The location and dimension of the fault steps along and at the ends of the earthquake ruptures and the distances to the nearest neighboring active fault traces from the end points of surface rupture

Table 1

Geological Observations

Date (mm/dd/yyyy)	Location	Number	Type*	Length (km)‡	$S^{\dagger}$(Average Net Slip) (m)	S^{max} Max Slip (m)	Depth (km)	Rigidity μ (10^{11} dyne cm^2)	M_0^G(10^{26} dyne cm)	P_0^G(10^{15} cm^3)	M_w^G	Reference§	Notes‖
01/09/1857	San Andreas, CA	1	SSR	360	4.7	9.1 (12)	15	3	76	25.4	7.9	1	a
05/03/1887	Sonora, MX	2	N/60	70	2.2	4.1	15	3	8.0	2.7	7.2	2, 3, 48	b
10/28/1891	Neo-Dani, Japan	3	SSL	80	3.1	7.9	15	3	11.3	3.8	7.3	4	c
08/31/1896	Rikuu, Japan	4	R/45	37	2.5 (3.5)	6.2 (8.8)	15	3.0	8.2	2.7	7.2	5	d
10/02/1915	Pleasant Valley, NV	5	N/45	61	1.8 (2.6)	5.8 (8.2)	15	3.1	10.3	3.4	7.3	6	e
11/02/1930	Kita-Izu, Japan	6	SSL	35	1.1	3.5	12	3.3	1.6	0.48	6.7	7	f
12/25/1939	Erzincan, Turkey	7	SSR	300	4.2	7.4	13	3.2	52.5	16.4	7.7	8	g
05/19/1940	Imperial, CA	8	SSR	60	1.6	3.3	13	2.5	3.0	1.2	6.9	9	h
12/20/1942	Erbaa-Niksar, Turkey	9	SSR	28	1.66	1.9	13	3.2	1.8	0.6	6.8	8	I
11/26/1943	Tosya, Turkey	10	SSR	275	2.5	4.4	13	3.2	28.7	9.0	7.6	8	j
09/10/1943	Tottori, Japan	11	SSL	10.5	0.6	1.5	15	3.3	0.3	0.09	6.3	10	k
02/01/1944	Gerede-Bolu, Turkey	12	SSR	155	2.1	3.5	13	3.2	13.3	4.2	7.35	8	l
01/31/1945	Mikawa, Japan	13	R/30	4.0	1.3	2.1	8	3.0	0.24	.08	6.2	11	m
12/16/1954	Fairview Peak, NV	15	NSSR/60	62	1.1	5.2	15	3.0	3.5	1.2	7.0	13	n
12/16/1954	Dixie Valley, NV	16	N/60	47	0.8 (0.9)	3.1 (3.5)	12	3.0	1.76	0.6	6.8	13	t
08/18/1959	Hebgen Lake, MT	14	N/50	25	2.5	5.4	15	3.0	3.7	1.25	7.0	12	s
07/22/1967	Mudurnu, Turkey	17	SSR	60	0.9	2.0	12	2.4	1.6	0.65	6.7	8	u
04/08/1968	Borrego Mtn, CA	18	SSR	31	0.13	0.4	12	3.3	0.16	0.05	6.1	14	v
02/09/1971	San Fernando, CA	19	R/45	15	0.95	2.5	15	3.4	1.0	0.30	6.7	59	ap
06/02/1979	Cadoux, Australia	20	R/35	10	0.6	1.2	6	3.2	0.20	0.06	6.1	49	x
10/15/1979	Imperial Valley, CA	21	SSR	36	0.28–0.41	0.6–0.78	13	2.5	0.33–0.48	0.13–0.19	6.3–6.4	15, 16	w
10/10/1980	El Asnam, Algeria	22	R/50	27.3	1.2	6.5	12	3.0	1.55	0.5	6.7	60	aq
07/29/1981	Sirch, Iran	23	SS/69	64	0.13	0.50	15	3.3	0.43	0.13	6.4	50	aj
10/28/1983	Borah Peak, ID	24	N/45	34	.94 (1.3)	2.8 (4.0)	14	3.2	2.9	0.89	6.9	17	y
03/03/1986	Marryat, Australia	25	R/35	13	0.24 (sec) (0.42)	0.70 (sec) (1.2)	3	3.2	0.09 (sec)	0.03 (sec)	5.9 (sec)	46	z
					0.26*u* (0.46)	0.8*u* (1.4)			0.10*u*	0.03*u*	5.9*u*		
03/02/1987	Edgecumbe, NZ	27	N/60	15.5	0.6 (0.7)	2.6 (3.0)	10	2.6	0.33	0.13	6.3	19	ao

(*continued*)

Table 1 (*Continued*)

Date (mm/dd/yyyy)	Location	Number	Type*	Length (km)‡	$S^{\dagger}$(Average Net Slip) (m)	S^{max} Max Slip (m)	Depth (km)	Rigidity μ (10^{11} dyne cm^2)	M_0^G(10^{26} dyne cm)	P_0^G(10^{15} cm^3)	M_w^G	Reference§	Notes‖
11/23/1987	Super. Hills, CA	26	SSR	25	0.3–0.6	0.5–1.1	12	2.5	0.22–0.47	.09–.19	6.2–6.4	18	aa
01/22/1988	Tennant Crk, Australia	28	R/45	30	0.7 (1.0)	1.8 (2.5)	8	3.3	1.1	0.34	6.6	43	ab
07/16/1990	Luzon, Philippines	29	SSL	112	3.5	6.2	20	3.5	27.4	7.84	7.6	20, 21	am
06/28/1992	Landers, CA	30	SSR	77	2.3	6.7	15	3.0	8.1	2.7	7.2	22	ac
03/14/1998	Fandoqa, Iran	31	SSN/54	25	1.1	3.1	10	3.3	1.2	0.36	6.6	50	ag
08/17/1999	Izmit, Turkey	34	SSR	107 (145)	1.1	5.1	13	3.2	4.9	1.5	7.1	47	ae
09/21/1999	Chi-Chi, Taiwan	32	R/70	72	3.5 (4.0)	12.7 (16.4)	20	3.0	18.4	6.1	7.4	23	ad
10/16/1999	Hector Mine, CA	33	SSR	44	1.56	5.2	12	3.0	2.5	0.82	6.9	57	an
11/12/1999	Duzce, Turkey	35	SSR	40	2.1	5.0	13	3.2	3.5	1.1	7.0	24	af
11/14/2001	Kunlun, China	36	SSL	421	3.3	8.7	15	3.0	62.5	20.8	7.8	53	am
11/14/2001 (spot)	Kunlun, China	36a	SSL	428	2.4	8.3	15	3.0	46.8	15.6.	7.8	61	al
11/03/2002	Denali, AK	37	SSR	302	3.6	8.9	15	3.2	51.6	16.1	7.7	52	ak

*Type of earthquake mechanism and dip. Right- and left-lateral strike slip are SSR and SSL, respectively. Reverse and normal events are R and N, respectively. Right-lateral normal oblique motion is NSSR.

†See column labeled Notes for an explanation of the calculation for each event. When two values are given, the value in rounded brackets is the calculated net slip and the other is for the type of slip provided in the original slip distribution.

‡The digitized distance along fault rupture trace.

§See Table 3 for the key to the references.

‖See Ⓔ the electronic edition of *BSSA* for notes bearing on the basis for assigning column values and location of the epicenter when plotted.

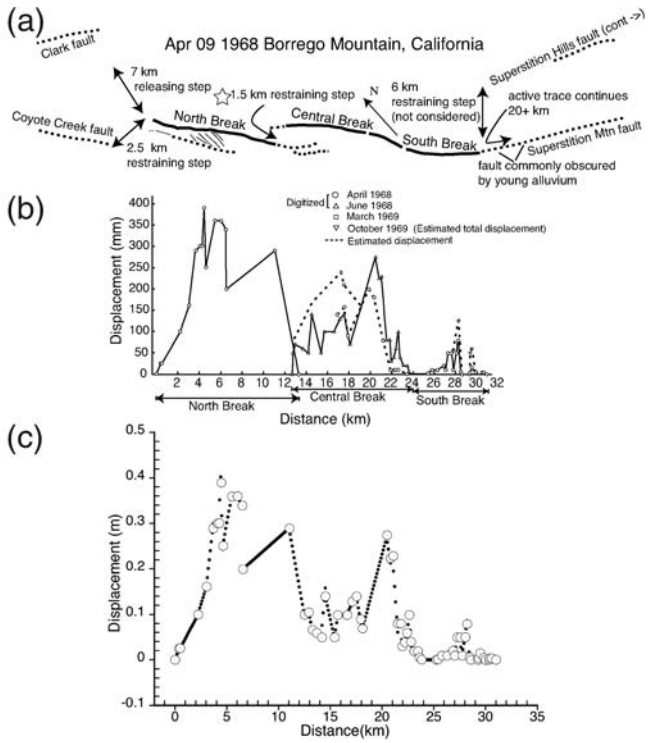

Figure 1. Illustration of data synthesis and analysis. (a) Map of 1968 Borrego Mountain earthquake rupture trace shown as bold lines. Adjacent and continuing traces of active faults that did not rupture during the earthquake are shown as thinner dotted lines. Also annotated are the dimensions of fault steps measured approximately perpendicular to the fault strike and the distance to the nearest-neighboring fault from the 1968 rupture end points. (b) Geologic measurements of surface slip along the rupture trace. (c) Plot of digitization of slip curve showing both field measurements (large circles) and interpolated values (small solid circles). Similarly annotated maps and plots for all earthquakes used in this study (Table 1) are compiled in Ⓔ the electronic edition of *BSSA*. References to map and slip curve sources are given in Table 1.

traces are annotated. The size of steps in the fault trace are generally taken as the distance between en echelon strands measured perpendicular to the average fault strike. Steps in the fault trace are also labeled as restraining or releasing depending on whether volumetric changes within the step resulting from fault slip would produce contractional or dilational strains within the steps, respectively (e.g., Segall and Pollard, 1980). The epicenter of the earthquake is also shown by a star. The maps and slip distributions for all of the earthquakes in Table 1 are presented in the same manner and collected in Ⓔ the electronic edition of *BSSA*. The resolution of the available maps generally limits observations to discontinuities of about 1 km and greater.

I have digitized and linearly interpolated between each of the original points in the slip distributions to form slip distribution curves at a resolution sufficient to reflect the details of the original slip measurements at either 0.1 or 1-km intervals (e.g., Fig. 1). The original and interpolated points of the slip curves for all earthquakes in Table 1 are presented both graphically and in tabular form in Ⓔ the electronic edition of *BSSA*.

The seismic moment M_0 is used here as the primary measure of the earthquake size and is equal to μLWS, where μ is the crustal rigidity of the rocks in which the earthquake occurs, L and W are, respectively, the length and width of the fault plane that produces the earthquake, and S is the coseismic slip during the earthquake (Aki and Richards, 1980). The value of M_0 may be determined from seismological or geodetic measures of seismic waves or ground deformations resulting from an earthquake, respectively. In such analyses, the value of rigidity μ is assumed independently from seismic velocity models that describe the crust in the vicinity of the earthquake source, and the depth D to which rupture extends is generally assigned as the depth of aftershocks or regional background seismicity. The value M_0 may also be determined primarily from geological observations where estimates of S and L have been obtained from field measurements of offsets along the surface expression of the causative fault. In this case, the measurement is limited to earthquakes large enough to break the ground surface and to those for which independently derived values of μ and W can be drawn from seismological observations. For convenience of discussion, estimates of M_0 determined in this latter manner are here labeled M_0^G and are referred to as geologic moments. Similarly, estimates of moment derived primarily from instrumental measurements are denoted M_0^{inst}.

The estimates of geologic moment M_0^G and the parameters from which the estimates are calculated are listed for each event in Table 1. Specifically, the digitized slip curves (Fig. 1 and Ⓔ the electronic edition of *BSSA*) are used to calculate the average S and maximum $S^{\max}$ coseismic surface slip and rupture length L for each listed event. The investigations on which values of the depth extent of rupture D, the rigidity μ, and the fault type (mechanism and dip δ) used to estimate the respective geologic moments are also referenced in Table 1. The basis for assigning the values of μ and rupture depth D for the respective earthquakes are described in further detail in the notes of Table 1. The value of rupture width W used in calculating M_0^G is $D/\sin(\delta)$, where δ is the dip and listed in the column labeled Type in Table 1. Because of uncertainties in the estimates of μ used in seismic moment calculations, it has been suggested that geometrical moment or seismic potency P_0, which is the seismic moment M_0 divided by the crustal rigidity μ, may provide a more fundamental scaling parameter for comparing the relative size of earthquakes (Ben-Menahem and Singh, 1981; Ben-Zion, 2001). To examine this idea, I calculate and list a value P_0 for each event.

Instrumentally derived estimates of the seismic moment M_0^{inst} of each event are listed in Table 2 when available. The sources of the estimates are cited and each denoted according to whether it was derived from seismic body waves, surface waves, or geodetic measurements. For each, I have also attempted to extract the value of rigidity μ used by investigators in calculating the instrumentally derived seismic

Table 2

Seismological Observations

Date (mm/dd/yyyy)	Location	Number	Type	M_0^{inst} M_0^{body} 10^{26} dyne cm	M_0^{inst} $M_0^{long\ period}$ 10^{26} dyne cm	M_0^{inst} $M_0^{geodetic}$ 10^{26} dyne cm	M_0^{inst} Range 10^{26} dyne cm	P_0^{inst} P_0^{body} 10^{15} cm^3	P_0^{inst} $P_0^{long\ period}$ 10^{15} cm^3	P_0^{inst} $P_0^{geodetic}$ 10^{15} cm^3	P_0^{inst} Range 10^{15} cm^3	References	Notes
10/02/1915	Pleasant Val, NV	5	N/60	2.7 ± 0.6 (3.3)			2.7 ± 0.6	0.82			0.82	27	be
11/02/1930	Kita-Izu, Japan	6	SSL			2.7 (3.3)	—			0.82	0.82	56	bak
05/19/1940	Imperial, CA	8	SSR	2.3 (3.3)	4.8 (3.3)	8.4 (3.3*)	5.3 ± 3.1	0.696	1.45	2.5	1.62 ± 0.92	42	bh
				3.0 (3*)				1.0		5			
				4.4 (3.3)				1.3					
09/10/1943	Tottori, Japan	11	SSL	3.6 (3.35)			3.6	1.08			1.08	40	bk
01/31/1945	Mikawa, Japan	13	R	1 (3)		0.87 (3)	0.94 ± 0.065	0.33		0.29	0.35 ± 0.05	41	bm
				1 (2.5)				0.40					
08/18/1959	Hebgen Lake, MT	14	N/500	10 (3.3)	15 (3)	13 (3.23)	12.5 ± 2.5	3.0	5.0	4.0	4.0 ± 1.0	31	bs
12/16/1954	Fairview Peak, NV	15	NSSR/60	5.5 (3)		4.6 (3.0)	5.05 ± 0.45	1.83		1.53	1.68 ± 0.15	35	br
12/16/1954	Dixie Valley, NV	16	N/60	1.0 (3.3)		2.2 (3.0)	1.6 ± 0.6	0.30		0.73	0.52 ± 0.22	36	bt
07/22/1967	Mudurnu, Turkey	17	SSR	8.8 (3.3)	7.5 (3*)		11.25 ± 3.75	2.67	2.5		3.75 ± 1.25	39	bu
				11 (2.4)				4.58					
				15 (3*)				5.0					
04/08/1968	Borrego Mtn, CA	18	SSR	0.9 (3)	1.1 (3*)		0.95 ± 0.25	0.3	0.37		0.29 ± 0.08	28	bv
				1.1 (3.4)				0.32					
				0.7 (3.3)				0.21					
				1.2 (3.8)				0.315					
02/09/1971	San Fernando, CA	19	R/45	1.3 (3*)	1.9 (3*)		1.4 ± 0.5	0.43	0.63		0.38 ± 0.15	59	bam
				0.9 (3.5)				0.23					
				1.7 (3.3)				0.52					
06/02/1979	Cadoux, Australia	20	R/35	0.15 (3.2)	0.175 (4.4)		0.163 ± 0.013	0.046	0.040		0.043 ± 0.0035	45	bx
10/15/1979	Imperial, CA	21	SSR	0.5 (2.5)	0.7 (3*)		0.61 ± 0.11	0.20, 0.20	0.233		0.233 ± 0.033	30	bw
				0.5(2.5)	0.72 (2.7)				0.267				
10/10/1980	El Asnam	22	R/50	2.5 (3)			2.5				0.83	60	ban
1981-Jul-29	Sirch, Iran	23	SS/54	3.7 (3.3*)	9.0 (4.4)		6.35 ± 2.65	1.12	2.05		1.58 ± .046	50	bah
10/28/1983	Borah Peak, ID	24	N/60	2.1 (3.3)	3.5 (3*)	2.6 (3.2)	2.8 ± 0.7	0.64	1.2	0.81	0.90	29	by
				2.3 (2.5)	3.1 (2.7)	2.9(3.2)		0.92	1.1	0.91	±0.27		
03/03/1986	Marryat, Australia	25	R/35	0.06 (3.2)			0.06	0.019			0.019	45	bz
11/23/1987	Superstition Hills, CA.	26	SSR	0.5 (3.3)	1.0 (3*)	0.9	0.6 ± 0.4	0.15	0.33	0.32	0.266 ± 0.18	33	baa
				0.8 (1.8)	0.7 (4.4)	(2.8)		0.44	0.16				
				0.2 (2.3)				0.09					
03/02/1987	Edgecumbe, NZ	27	N/60	0.4 (3.5)	0.9 (3.6)		0.65 ± 0.25	0.11	0.25		0.182 ± 0.067	34	bai
				0.7 (3.6)	0.6 (4.4)			0.19	0.14				
01/22/1988	Tennant Creek, Australia	28	R/45	1.6 (3.3)	1.5 (4.4)		1.55 ± 0.05	0.48	0.35		0.41 ± 0.07	44	bab

(*continued*)

Table 2 (*Continued*)

Date (mm/dd/yyyy)	Location	Number	Type	M_0^{inst} M_0^{body} 10^{26} dyne cm	$M_0^{long\ period}$ 10^{26} dyne cm	$M_0^{geodetic}$ 10^{26} dyne cm	Range 10^{26} dyne cm	P_0^{inst} P_0^{body} 10^{15} cm^3	$P_0^{long\ period}$ 10^{15} cm^3	$P_0^{geodetic}$ 10^{15} cm^3	Range 10^{15} cm^3	References	Notes
07/16/1990	Luzon, Philippines	29	SSL	36 (4.0)	39 (7.3)		38.5 ± 2.5	9.0, 5.3	9.3		7.3 ± 2.0	32	baj
					41 (4.4)								
06/28/1992	Landers, CA	30	SSR	7 (3*)	8 (3*)	9 (3.0)	8.8 ± 1.8	2.3	2.7	3.0	2.8 ± 0.5	25	bac
				7.5 (3)	10.6 (4.4)	10 (3*)		2.5	2.4	3.3			
03/14/1988	Fandoqa, Iran	31	SSN	0.9 (3.3)	0.95 (4.4)	1.2 (3.4)	1.05 ± 0.15	0.28	0.22	0.35	0.284 ± 0.07	50	bag
09/20/1999	Chi-Chi, Taiwan	32	R/70	29 (2.1)	34 (4.4)	27 (3)	34 ± 7	13.8	7.7	9.0	10.8 ± 3.0	26	bad
				41 (3.0)				13.7					
10/16/1999	Hector Mine,CA	33	SSR	6.2 3*)	6.0 (4.4)	6.8 (3*)	6.45 ± 0.55	2.1	1.4	2.3	1.8 ± 0.45	58	bal
						5.9 (3*)				2.0			
						7.0 (3.0)				2.3			
08/17/1999	Izmet, Turkey	34	SSR	22 (3.3	28.8 (4.4)	24 (3.3)	21.9 ± 6.9	6.7	6.6	7.3	5.97 ± 1.7	38	bae
				15 (3.5)		18 (3.3)		4.3		5.4			
						26 (3.4)				7.7			
11/12/1999	Duzce, Turkey	35	SSR	5.0 (3*)	6.7H (4.4)	5.4 (3.0)	5.4 ± 1.3	1.67	1.52	1.80	1.66 ± 0.14	37	baf
11/14/2002	Kunlun, China	36	SSL	46 (3)	59 (4.4)	71 (3 *)	58.5 ± 12.5	15.3, 16.7	13.4	23.6	18.5 ± 5.1	55	bai
				50 (3.0)									
11/032002	Denali, AK	37	SSR	68 (3.3)	75 (2.6)		56.5 ± 18.5	20.1	28.8		20.7 ± 8.1	54	baj
				38 (3*)				12.7					
				49 (3*)				16.3					
				56 (3)				18.7					

See Ⓔ the electronic edition of *BSSA* for notes and references bearing on assignment of rigidity.

Table 3

References Cited in Tables 1 and 2

Number Used in Tables 1 and 2	Reference Cited
1	Sieh, 1978
2	Bull and Pearthree, 2002
3	Pezzopane and Dawson, 1996
4	Matsuda, 1974
5	Matsuda *et al.*, 1980
6	Wallace, 1980
7	Matsuda, 1972
8	Barka, 1996
9	Trifunac and Brune, 1970
10	Kaneda and Okada, 2002
11	Tsuya, 1946
12	Witkind, 1964
13	Caskey *et al.*, 1996
14	Clark, 1972
15	Johnson and Hutton, 1982
16	Sharp *et al.*, 1982
17	Crone *et al.*, 1987
18	Sharp *et al.*, 1989
19	Beanland *et al.*, 1989
20	Nakata, 1990
21	Yomogida and Nakata, 1994
22	Sieh *et al.*, 1993
23	Lin *et al.*, 2001
24	Akyuz *et al.*, 2002
25	Cohee and Beroza, 1994; Dreger, 1994; Freymueller, 1994; Johnson *et al.*, 1994; Wald and Heaton, 1994
26	Chi *et al.*, 2001; Wu *et al.*, 2001; Zeng and Chen, 2001
27	Doser, 1988
28	Hanks and Wyss, 1972; Burdick and Mellman, 1976; Heaton and Helmberger, 1977; Swanger *et al.*, 1978; Ebel and Helmberger, 1982; Butler, 1983; Vidale *et al.*, 1985
29	Hanks and Wyss, 1972; Doser and Smith, 1985; Tanimoto and Kanamori, 1986; Ward and Barrientos, 1986; Mendoza and Hartzell, 1988
30	Hartzell and Helmberger, 1982; Kanamori and Reagan, 1982; Hartzell and Heaton, 1983; Doser, 1990
31	Doser and Smith, 1985; Barrientos *et al.*, 1987; Doser and Kanamori, 1987
32	Yoshida and Abe, 1992; Velasco *et al.*, 1996
33	Dziewonki *et al.*, 1989; Frankel and Wennerberg, 1989; Sipkin, 1989; Hwang *et al.*, 1990; Wald *et al.*, 1990; Larsen *et al.*, 1992
34	Priestly, 1987; Anderson and Webb, 1989
35	Doser, 1986; Hodgkinson *et al.*, 1996
36	Doser, 1985; Hodgkinson *et al.*, 1996
37	Burgmann *et al.*, 2002; Umutlu *et al.*, 2004
38	Delouis *et al.*, 2002; Li *et al.*, 2002; Sekiguchi and Iwata, 2002
39	Hanks and Wyss, 1972; Stewart and Kanamori, 1982; Taymaz *et al.*, 1991; Pinar *et al.*, 1996
40	Kanamori, 1973
41	Ando, 1974; Kakehi and Iwata, 1992; Kikuchi *et al.*, 2003
42	Trifunac, 1972; Thatcher and Hanks, 1973; Reilinger, 1984; Doser and Kanamori, 1987; Doser, 1990
43	Crone *et al.*, 1992
44	Choy and Bowman, 1990
45	Fredrich *et al.*, 1988
46	Machette *et al.*, 1993
47	Barka *et al.*, 2002
48	Suter and Contreras, 2002
49	Lewis *et al.*, 1981
50	Berberian *et al.*, 2001
51	Eberhart-Phillips *et al.*, 2003
52	Haeussler *et al.*, 2005
53	Lin *et al.*, 2002; Xu *et al.*, 2002; Klinger *et al.*, 2005
54	Choy and Boatwright, 2004; Frankel, 2004; Ozacar and Beck, 2004
55	Antolik *et al.*, 2004; Ozacar and Beck, 2004; Lasserre *et al.*, 2005
56	Abe, 1978
57	Treiman *et al.*, 2002
58	Ji *et al.*, 2002; Jonsson *et al.*, 2002; Kaverina *et al.*, 2002
59	Allen *et al.*, 1971; Wyss, 1971; Allen *et al.*, 1975; Langston, 1978; Heaton, 1982
60	Yielding *et al.*, 1981
61	Klinger *et al.*, 2006

moment values. The values of rigidity μ are then used to convert the measures of seismic moment to potency P_0. The original references and notes describing the basis for the values of rigidity used in each of the moment calculations are provided in the notes accompanying Table 1. These data are also the basis for the values of μ used in calculating the geologic moments of the respective earthquakes in Table 1.

Observations

The data set is limited to continental earthquakes. Thirty-seven earthquakes are listed in Table 1. Twenty-two are primarily strike slip, seven are normal slip, and the remaining eight are reverse slip. The following section presents the observations summarized in Tables 1 and 2 graphically. The implications of the observations are then discussed in the subsequent section. The plots are designed to illustrate how variables in the data set scale with one another. Curves are fit when applicable to the observations to quantify the relationships. For each plot, the type of curve (e.g., linear, log linear, power law), the parameters leading to the best fit of the curve to the data, and the number of data points are defined within the plot space. The quality of curve fits are also variously described by values of Pearson's regression coefficient R, chi-square, and standard deviation (Press *et al.*, 1992).

Rupture Width and Aspect Ratio

Rupture width W is plotted versus surface rupture length and both the geologic and instrumental moment in Figure 2. Each plot shows that widths of strike-slip ruptures on vertical or near-vertical faults are generally assigned values between 10 and 15 km, the width of the seismogenic layer in continental environments. The rupture widths for the strike-slip earthquakes are thus largely independent of earthquake size though examination of the plots allows the suggestion that widths of larger earthquakes tend to be more frequently characterized by relatively larger values of W than do lesser earthquakes in the data set. Because normal faults dip at relatively smaller angles through the seismogenic layer, the rupture widths tend to be larger and reach ~20 km in width, with the exception of the 1987 Edgecumbe earthquake (event 27) that occurred in the Taupo Zone of New Zealand, a region of particularly high heat flow (e.g., Rowland and Sibson, 2004). The range of fault widths is greater for reverse faults, ranging from about 5 to 20 km. Three of the eight reverse faults in the data set occurred in the intraplate environment of Australia (events 20, 25, and 28) where rupture depths have been observed to be particularly shallow (Langston, 1987; Fredrich *et al.*, 1988; Choy and Bowman, 1990). The three Australian intraplate events define the lower end of the range in both W and L values for the eight reverse type earthquakes and appear responsible for the apparent positive relationship between L and W for reverse type earthquakes.

The same data are recast in a plot of the aspect ratio (rupture length per rupture width, L/W) versus the rupture length in Figure 3a. The best-fitting curve of form

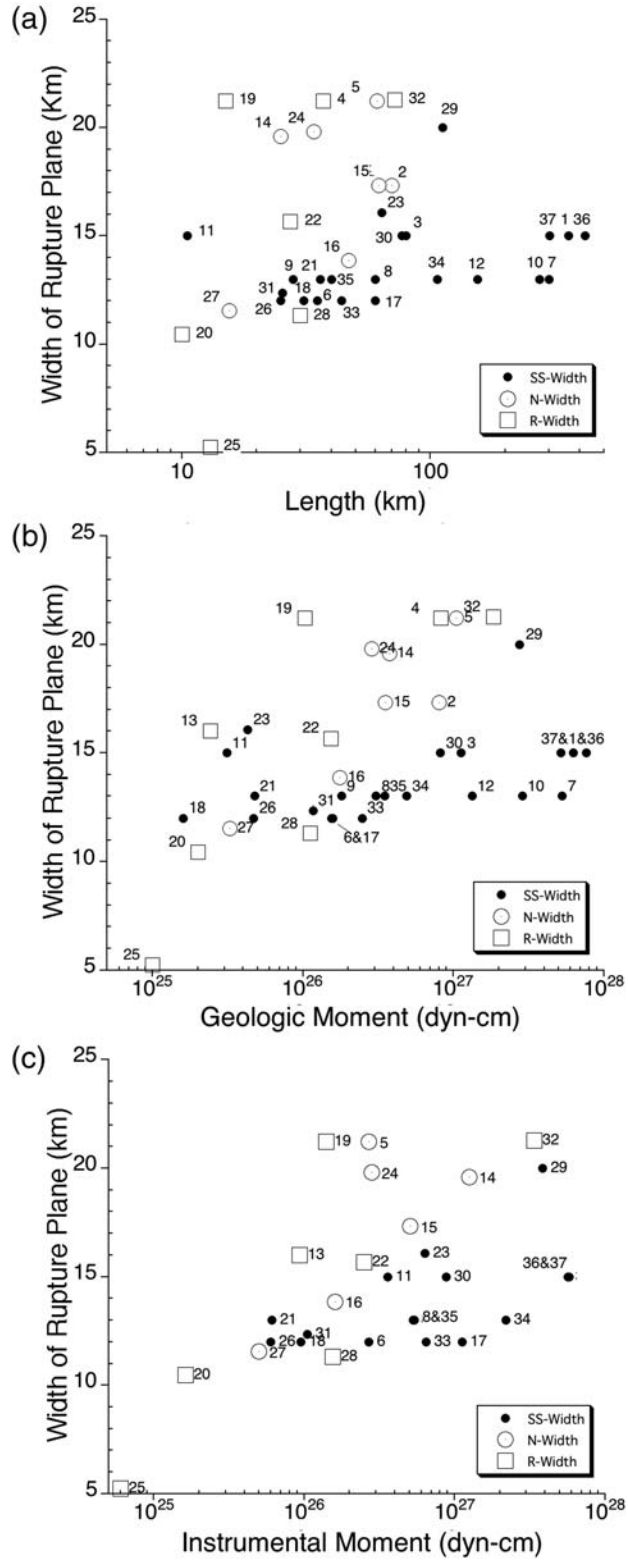

Figure 2. Rupture width as a function of (a) rupture length, (b) geologic moment, (c) instrumentally derived seismic moment for events in Table 1. The 1945 Mikawa (13) and 1999 Izmit (34) rupture lengths are minimum because they do not include offshore extent of rupture.

aspect ratio $= A \times L^B$ to the strike-slip data is characterized by a value of $B = 1$, indicating a linear relationship between aspect ratio and rupture length. The value $B = 1$ is that which would be expected by limiting the depth extent of earthquake ruptures to a seismogenic layer of relatively constant thickness. The normal fault ruptures are similarly characterized but tend to fall below the strike-slip events. This latter difference arises because the events share a seismogenic layer of about the same thickness but the normal faults dip through the layer in contrast to the vertical planes of strike-slip ruptures. The reverse fault data show a similar tendency for aspect ratio to increase with length but the scatter in the fewer data yield a poorly fit regression. The aspect ratio is also plotted and similarly fit to regression curves as a function of M_0^G and M_0^{inst} in Figures 3b,c, respectively. In these cases, the same patterns arise but the increased scatter in the data leads to poorer curve fits. The greater scatter is because estimates of M_0 also incorporate uncertainties and variations in estimates of coseismic displacement S and rigidity μ between the respective earthquakes. The comparison of M_0^G to the aspect ratio in Figure 3b is somewhat circular in reasoning in that both M_0^G and aspect ratio are functions of L. Nonetheless, limiting comparison of rupture length to instrumental moment M_0^{inst} does not appear to significantly decrease the scatter in the relationship (Fig. 3c).

Instrumental versus Geologic Measures of Earthquake Size: Moment and Potency

The range of instrumentally derived values of seismic moment M_0^{inst} and potency P^{inst} generally span a range of a factor of 2–3 for the earthquakes listed in Table 2 (Fig. 4). Geological estimates of M_0^G generally fall within the range of instrumental estimates for the larger events in the data set (Fig. 4). The same is also illustrated in Figure 5 where the geologic estimates of seismic moment and potency are plotted as a function of the instrumentally derived values for the respective events. A solid line of slope 1 is drawn on each plot. The bounding dashed parallel lines fall a factor of 2 in geologic moment from the line of slope 1. Data points falling on the solid line of slope 1 would indicate perfect agreement between the geological and instrumental measures. The vertical error bars with each data point span a factor of 3 about the value of geologic moment. The horizontal error bars for each data point encompass the spread of instrumentally derived values given for each event and are plotted in Figure 4. The majority of the geologic estimates fall within a factor of 2 of the instrumental measures. Those with the greatest discrepancy tend to fall well below the respective instrumental measures, indicating that coseismic slip was probably concentrated at depth for the particular events. For only one event (the 1915 Pleasant Valley earthquake [event 5]) do the geologic estimates fall well above the instrumental estimates. Doser (1988) points out the discrepancy may be due in part to problems in the calibration of seismometers or because energy release during that earthquake occurred at longer

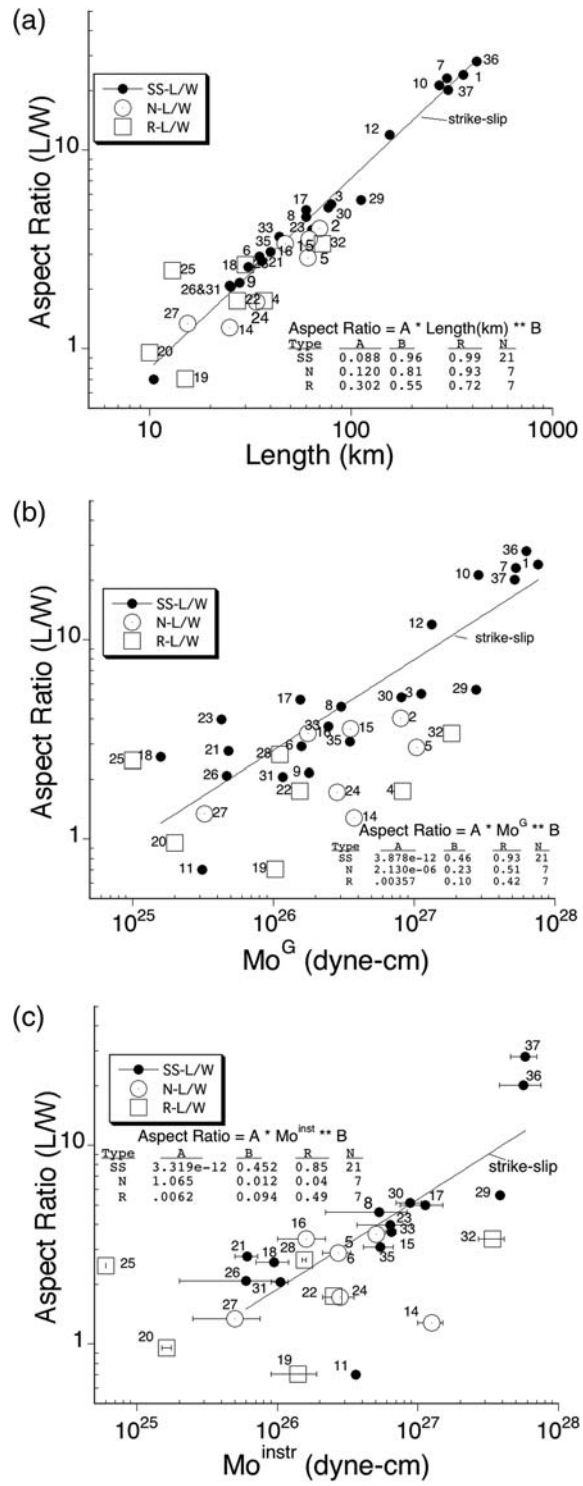

Figure 3. Aspect ratio (L/W) as a function of (a) surface rupture length (L) and moment M_0 derived from (b) geological and (c) instrumental measurements, respectively. Numbers correspond to events listed in Table 1. Horizontal bars in (c) represent the range of seismic moments reported by independent investigators and listed in Table 2. Parameters describing regression of the power-law curve for strike-slip, normal, and reverse faults are listed separately. Regression curve is shown only for strike-slip faults. The 1945 Mikawa and 1999 Izmet extend offshore and are not plotted or included in regressions.

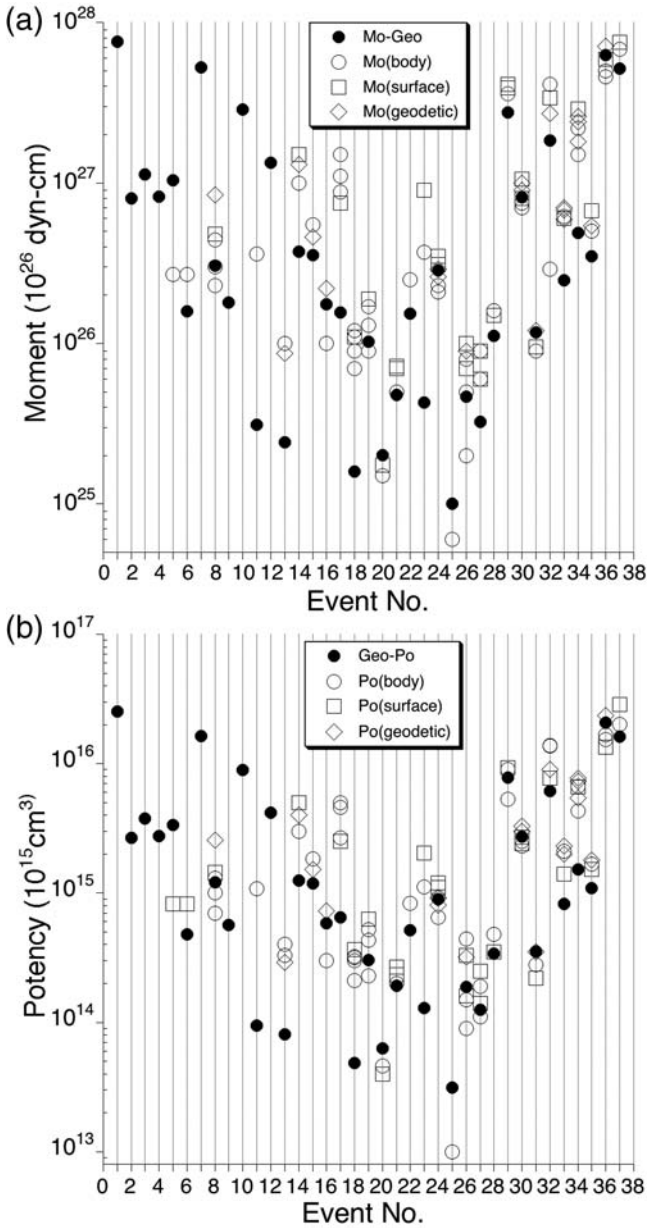

Figure 4. Geologically and instrumentally derived (a) seismic moments and (b) potencies plotted versus event number for earthquakes listed in Tables 1 and 2. Geologic values for events (13) (1945 Mikawa) and (34) (1999 Izmit) do not include portions of faults that extended offshore and are for that reason minimum values.

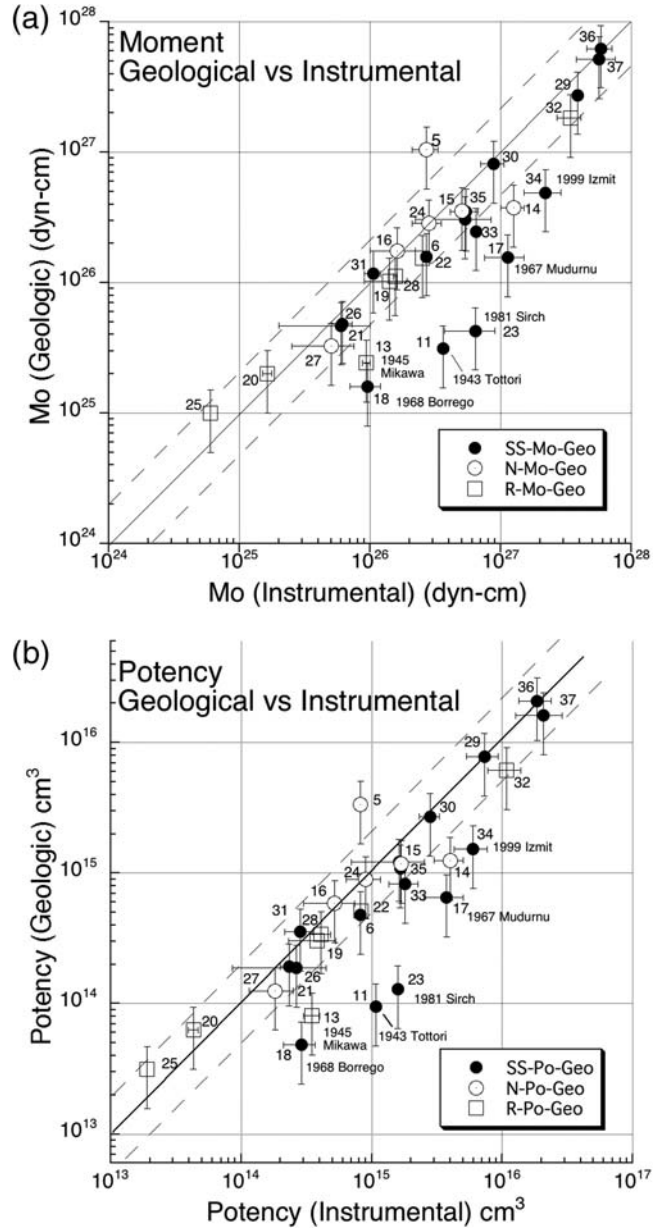

Figure 5. Geologically versus instrumentally derived estimates of (a) moment and (b) potency. Vertical bars span a factor of 3 in geologic moment. Horizontal bars reflect the spread of multiple measures of seismic moment reported by independent investigators. Perfect correlation would follow the solid line of slope 1. Dashed lines span a factor of 3 about the solid line of slope 1. The number next to each symbol corresponds to the listing of events in Table 1.

periods than recorded by the few seismograms available for analysis of the event.

Maximum versus Average Coseismic Slip

The ratio of the average to maximum values of slip listed in Table 1 is plotted as a function of rupture length and event number in Figure 6a. The ratio for all of the events regardless of mechanism is characterized by an average value of 0.41 with a standard deviation of 0.14. The subsets of strike-slip, reverse, and normal mechanisms show ratios of 0.44 ± 0.14, 0.35 ± 0.11, and 0.34 ± 0.10, respectively (Fig. 6b). No clear dependence of the ratio on rupture length is observed.

Coseismic Slip versus Rupture Length (Average and Maximum)

The average and maximum values of coseismic slip as a function of surface rupture length are shown in Figure 7. Linear curve fits are applied separately to each of the reverse,

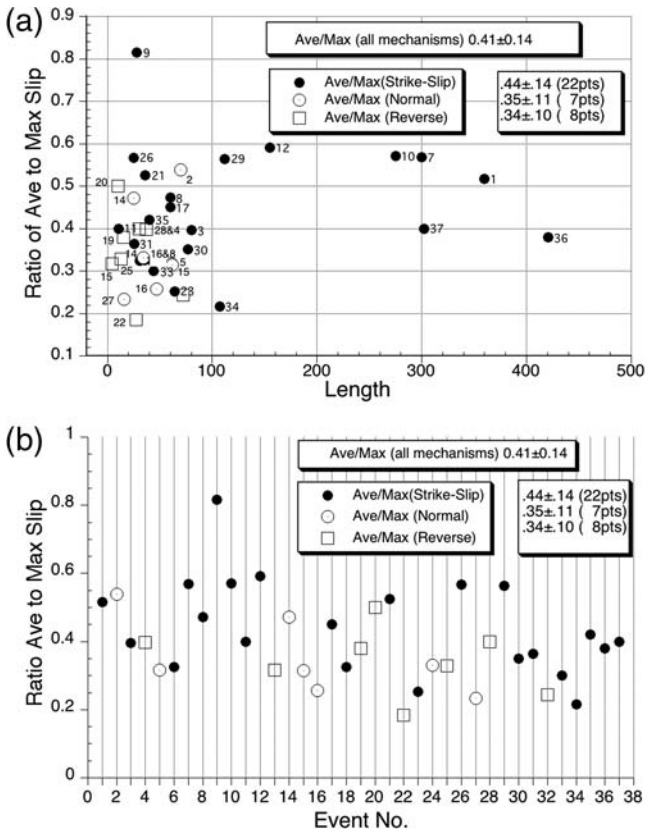

Figure 6. Ratio of average to maximum surface slip as function of (a) rupture length and (b) event number. Data point symbols differ according to the fault mechanism. The average value of ratio, standard deviation, and number of points (pts) are given in the key. Event numbers correspond to the earthquakes listed in Table 1.

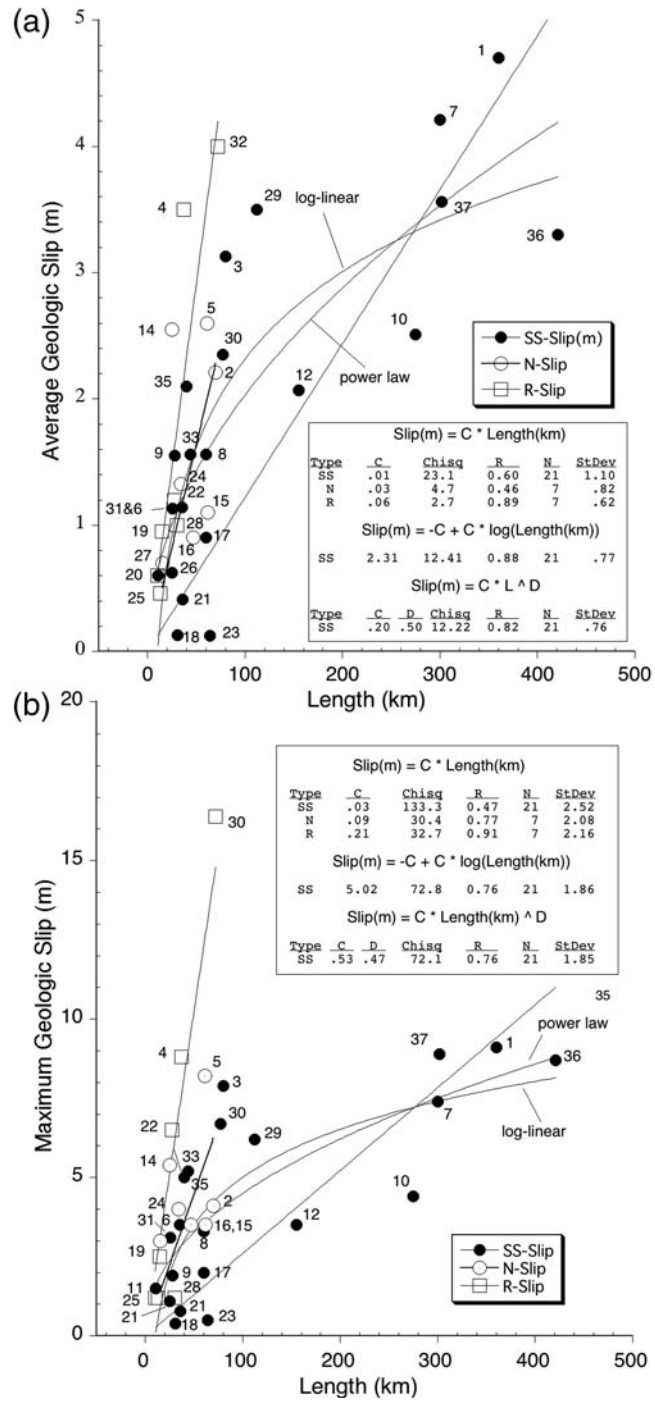

Figure 7. (a) Average and (b) maximum values of coseismic surface slip versus rupture length for earthquakes listed in Table 1. The 1945 Mikawa earthquake and 1999 Izmit earthquake ruptures extended offshore and are not included. Values are measured from digitized slip distribution curves.

normal, and strike-slip earthquakes. The slopes of the linear curve fits are increasingly greater for the strike-slip, normal, and reverse faults, respectively. While the reverse and normal fault observations appear reasonably well fit by a straight line, the strike-slip data are not. For this reason, I have further fit log-linear ($S[\mathrm{m}] = -C + C \log L[\mathrm{km}]$) and power-law ($S[\mathrm{m}] = CL^D[\mathrm{km}]$) curves to the strike-slip data. The log-linear fit is formulated to constrain the curve to intersect the point where both L and S are zero. These latter curves result in a significant reduction in formal uncertainties of the curve fit to the strike-slip data as compared to a straight line. The formal measures of uncertainty for the power-law and log-linear curve fits are virtually equal. The slopes of the lines describing the increase of slip show a decrease in slope as a function of rupture length without apparently reaching a plateau.

Instrumental Moment and Moment-Magnitude versus Rupture Length

Figure 8 shows the relationships of M_0 and M_w to L for the subset of events studied by instrumental means and listed in Table 2. Each shows a systematic increase with L though with significant scatter when viewing the entirety of the data set. The fewer number of observations and limited range of rupture lengths is insufficient to lend confidence to similar regressions for the subset of normal and reverse earthquakes as compared to strike-slip earthquakes.

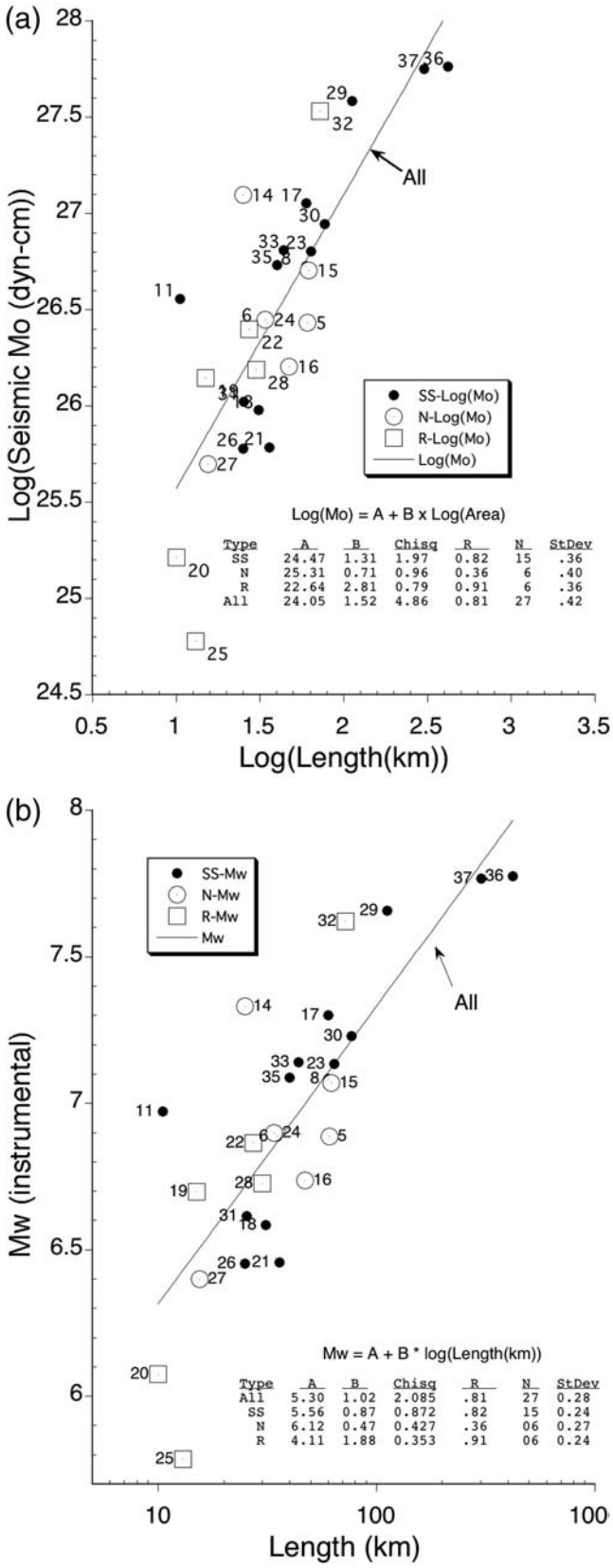

Figure 8. Instrumental measures of (a) M_w and (b) $\log(M_0)$ versus rupture length L and $\log(L)$, respectively, for the earthquakes listed in Table 1.

Shape of Surface Slip Distributions

To examine whether or not earthquake surface-slip distributions are characterized by any regularities in shape, I have fit various regression curves to the digitized slip distributions of the earthquakes listed in Table 1. The approach is illustrated in Figure 9, where three of the digitized surface-slip distributions are displayed along with a set of six best-fit regression curves. The simplest curve form is that of a flat line and yields the average displacement of the slip distribution. Additionally, curves of the form of a sine and ellipse are fit to the data. In these latter cases, the length is defined by the length of the surface rupture, the curve fits by form are symmetric, and the only free variable in fitting the curves to the observed slip distribution is the amplitude or maximum slip of the curve. Finally, I fit three curves allowing the shape of the fit to be asymmetric. These include a triangle, an asymmetric sine, and an asymmetric ellipse curve. The asymmetric sine and ellipse curves are defined by the shapes of the respective functions multiplied by a value $(1 - m \times (x/\mathrm{L}))$, where x is the distance along the fault, L is the rupture length, and m is a variable of regression. The multiplication reduces the amplitude of the sine and ellipse curves as a linear function of distance along the slip curve. In each of the asymmetric curve fits, there are then two variables of regression. For the triangle, the two variables of regression may be viewed as the slopes of the two lines that form the triangle, and it is the parameter m and the amplitude of the ellipse and sine functions for the asymmetric ellipse and asymmetric sine functions. Similar plots are provided for the digitized slip distributions of all events in Ⓔ the electronic edition of *BSSA*.

Each of the curve fits may be characterized by a standard deviation about the predicted value. Division of the standard deviation by the average value of the surface-slip distribution for the respective slip curves defines the coefficient of variation (COV) along the fault strike. The higher the value of COV, the poorer the curve fit. The COVs of the curve fits to each slip distribution are presented for comparison in Figure 10. The solid symbols represent values for the asymmetric curve fits and the open symbols are values for the flat line, symmetric sine, and ellipse curves. The plots show that the asymmetric functions consistently yield a better fit to the observations, and the flat line consistently yields the worst fit. Among the various asymmetric curve fits, none provide a consistently better fit to the data than the other. In sum, one may infer that surface-slip distributions are in general characterized by some degree of asymmetry, with the recognition that the relatively better fit of the asymmetric functions overall is largely the result of allowing the variation of two rather than one variable in the process of fitting curves to the observations.

The asymmetry of the resulting curve functions is depicted in Figure 11. Asymmetry is here defined as the ratio A/L, where A is the shortest distance from a rupture end point to the point of maximum slip (or median value of M_0 in

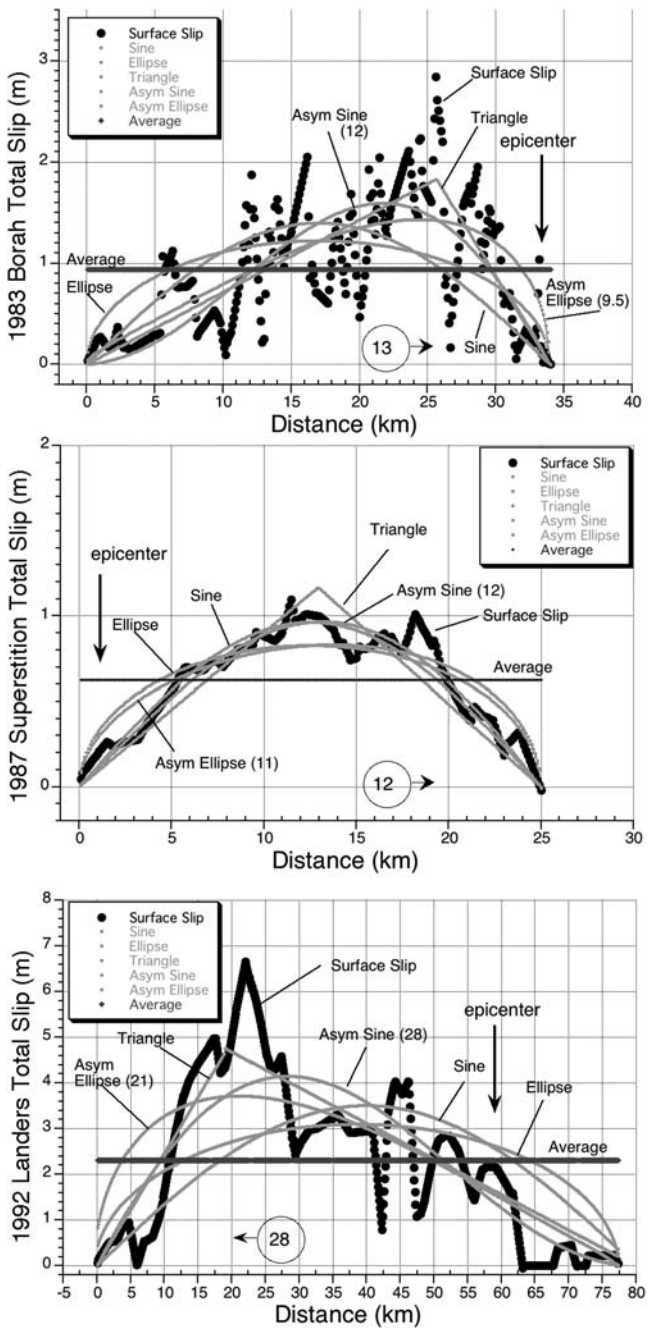

Figure 9. Examples of best-fitting regression curves to the coseismic surface-slip distributions for three of the earthquakes in Table 1. The digitized surface slip and respective types of regression curves are labeled in each plot. The position of the epicenter with respect to the fault strike is indicated by the downward pointing arrow. The integration of the digitized values of surface slip allows the definition of a point where half of the cumulative slip falls on either side. That value is defined for each slip distribution (values in circle) by the distance in kilometers to the nearest fault end point. The distances (in kilometers) of the peak values to the nearest end of the fault rupture are given in parentheses for the asymmetric sine and the asymmetric ellipse curve fits. The remaining events in Table 1 are analyzed in the same manner and are compiled in Ⓔ the electronic edition of *BSSA*.

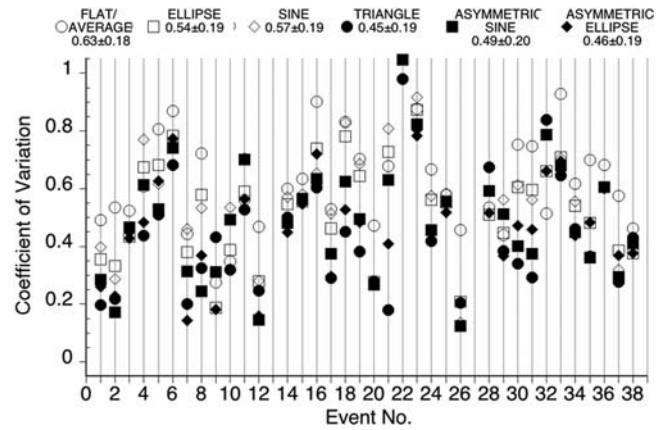

Figure 10. The COV for various curve fits to surface-slip distributions plotted as function of the number of the respective earthquake listed in Table 1. Average values and standard deviations are listed for each type of curve fit in the plot header. Asymmetric sine, ellipse, and triangle curves (solid symbols) consistently provide better estimation (lower COV) of observed slip distributions than do the flat line or symmetric sine and ellipse curves (open symbols).

the case of Fig. 11d) and L is the length of the rupture. It is observed that the degree of asymmetry one associates with a rupture is dependent on the shape of the curve assumed to best reflect the shape. The triangular function (Fig. 11a) tends to often enhance or increase the apparent asymmetry as compared to the asymmetric ellipse (Fig. 11b) and asymmetric sine functions (Fig. 11c). The same may be said for asymmetric ellipse as compared to the asymmetric sine functions. Finally, yet generally lesser values of asymmetry are defined when the reference to asymmetry is taken as the median value of M_0 (Fig. 11d).

Location of Epicenter in Relation to Shape of Slip Distribution

The spatial relationship of the location of earthquake epicenters to the shape of the slip distributions is illustrated with the plots in Figure 12. As in Figure 11, the asymmetry of the surface slip (solid symbols) is defined as the ratio A/L, where A is the shortest distance from a rupture end point to the peak slip (or median value of M_0, Fig. 12d) and L is the respective rupture length. Additionally, the relative location of the epicenter (open symbols) is defined by the ratio E/L, where E is the distance of the epicenter from the same respective rupture end point used to define A. In this manner, the ratio A/L is limited to between 0 and 0.5, whereas the ratio of E/L is limited between 0 and 1. The design of the plot is such that the open and closed symbols fall close together when the epicenter falls close to the maximum value of the slip function. Conversely, separation of the symbols indicates that the rupture initiated well away from the maximum value of the slip functions or the median value of M_0 in the case of Figure 12d. Values of E/L (open symbols) near zero or one indicate primarily unilateral rupture. Regardless of the shape of the curve fit assumed, there is not a systematic

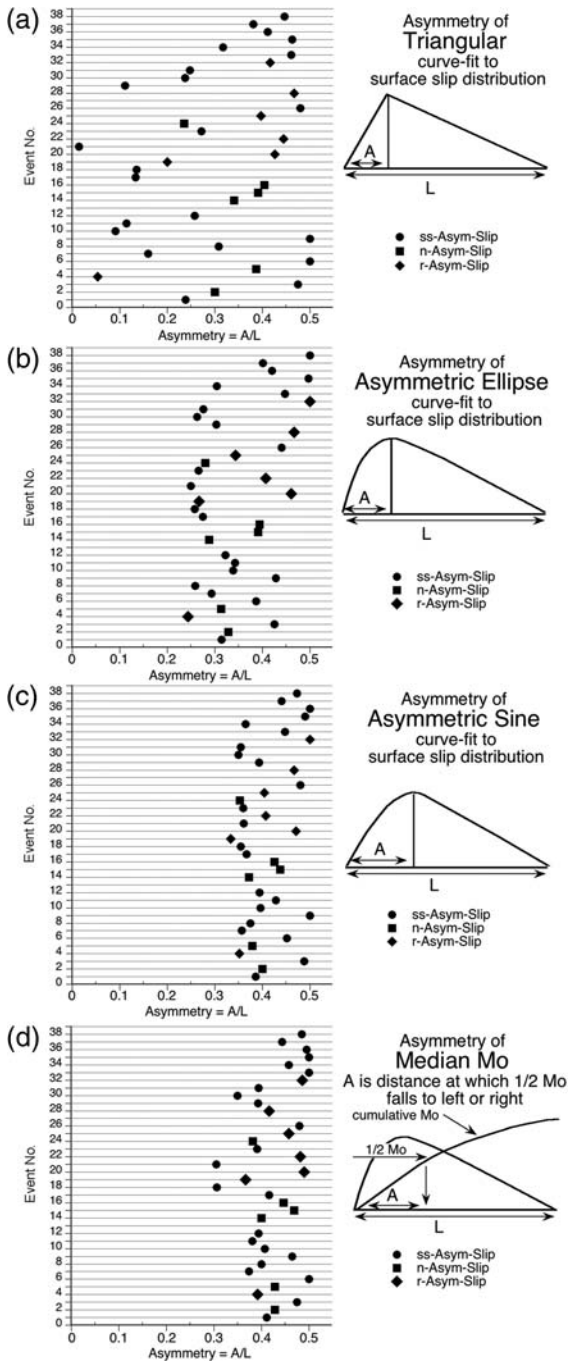

Figure 11. Asymmetry of earthquake surface-slip distributions for the earthquakes listed in Table 1 as defined with curve fits to the observed surface-slip distributions using (a) triangular, (b) asymmetric ellipse, (c) asymmetric sine functions, and (d) the point along the strike where the contribution of slip to seismic moment is divided equally along the strike. The asymmetry function is defined as the ratio A/L, where A is the shortest distance from a rupture end point to the peak slip or in the case of (d) where the contribution of slip to seismic moment is divided equally along the strike, and L is the respective rupture length. The function as defined is limited to between 0 and 0.5, whereby a value of 0 indicates the peak slip at the end point of rupture and 0.5 indicates the peak slip at the rupture midpoint. Different symbols are used for strike-slip (circles), normal (squares), and reverse (triangles) earthquakes.

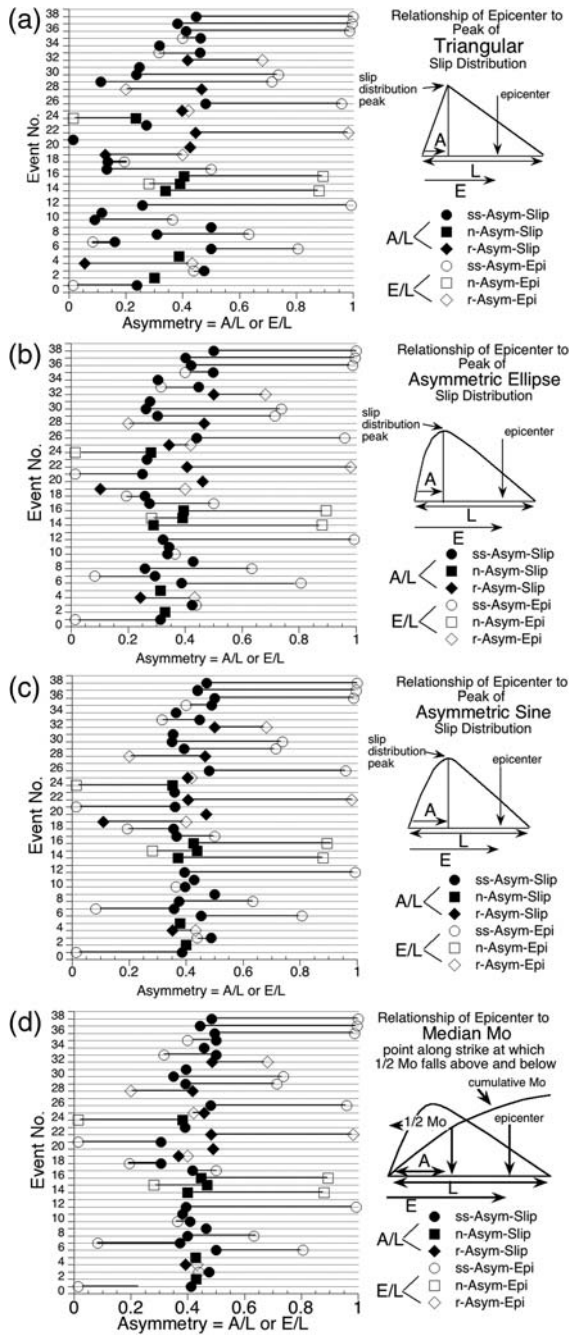

Figure 12. The relationship of epicenter location to asymmetry of surface-slip distributions as reflected in curve fits to surface-slip distributions using (a) triangular, (b) asymmetric ellipse, (c) asymmetric sine functions, and (d) point along the strike where contribution of slip to moment value is divided equally. The asymmetry of the surface slip (solid symbols) is defined as the ratio A/L, where A is the shortest distance from a rupture end point to the peak slip and L is the respective rupture length. The relative location of the epicenter is defined by the ratio E/L, where E is the distance of the epicenter from the same rupture endpoint used to define A. In this manner, the ratio A/L is limited to between 0 and 0.5, and the ratio E/L is limited to between 0 and 1. Strike-slip (ss), normal (n), and reverse (r) mechanisms are denoted by the appropriate symbols.

correlation of epicenter with the maximum slip value observed along the strike.

Shape of Surface-Slip Distribution as a Function of Rupture Length

Plots of the peak amplitudes of the various curves fit to the surface-slip distributions versus rupture length shown in Figure 13 provide another manner to characterize the shapes of the slip distributions. The plots show the same characteristics as observed in the earlier plots of surface slip versus rupture length presented in Figure 7a,b. Specifically, the fewer number of normal and reverse earthquake data may be fit by a straight line but the strike-slip earthquakes that cover a wider range of rupture lengths cannot. The observations for the strike-slip earthquakes (or the data set when taken as a whole) are better fit by curves that decrease in slope as a function of increasing rupture length. The result is the same regardless of the slip function (e.g., asymmetric sine or ellipse) assumed for each of the respective five plots.

Fault Trace Complexity and Earthquake Rupture Length

Strike-Slip Earthquakes. Examining maps of the earthquake surface rupture trace and nearby active fault traces that did not rupture during the earthquake such as shown for the 1968 Borrego Mountain event (Fig. 1a) provides a basis to

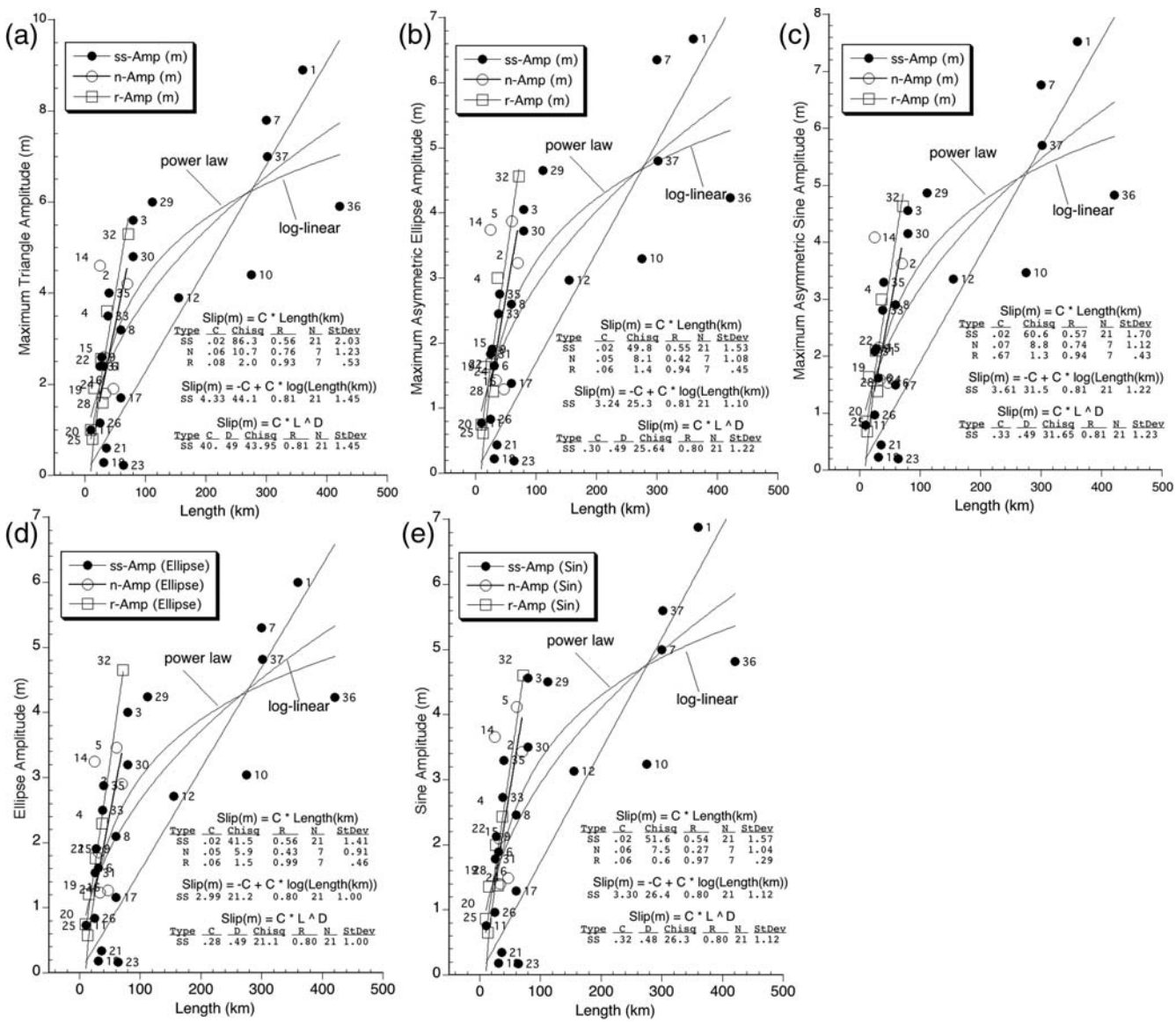

Figure 13. The maximum amplitude versus rupture length for (a) triangular, (b) asymmetric ellipse, (c) asymmetric sine, (d) ellipse, and (e) sine curve fits to digitized slip distributions of the earthquakes listed in Table 1. Events (13) (Mikawa) and (34) (Izmit) extended offshore and are not included in the plots or regressions.

examine the relationship between earthquake rupture length and fault trace complexity. The 1968 earthquake rupture, for example, (1) propagated across a 1.5-km restraining step, (2) stopped at a 2.5-km restraining step or 7-km releasing step at its northwestern (left) limit, and (3) died at its southeastern (right) limit in the absence of any geometrical discontinuity and at a point where the active trace can be shown to continue uninterrupted for 20 km or more past the end of the rupture. Figure 14 is a synopsis of the relationship between the length of rupture and the geometrical discontinuities for all strike-slip earthquakes listed in Table 1; it is largely the same as presented in Wesnousky (2006).

The vertical axis in Figure 14 is the dimension distance in kilometers. Each of the strike-slip earthquakes listed in Table 1 is spaced evenly and ordered by increasing rupture length along the horizontal axis. A dotted line extends vertically from each of the labeled earthquakes. Various symbols that summarize the size and location of geometrical steps within and at the end points of each rupture as well as where earthquake ruptures have terminated at the ends of active faults are plotted along the dotted lines. The symbols denote the dimension (in kilometers) of steps in surface rupture traces along the strike or the closest distance to the next mapped active fault from the terminus of the respective ruptures. Separate symbols are used according to whether the steps are releasing or restraining in nature, and whether they occur within (open squares and diamonds) or at the end points of the rupture trace (large solid symbols). In certain instances, the end points of rupture are not associated with a discontinuity in the fault strike, in which case the end point of rupture is denoted by a separate symbol (gray circles) and annotated with the distance that the active trace continues beyond the end point of rupture. As well, some earthquakes show gaps in surface rupture along strike and these are depicted as small solid dots. Because of the complexity of some ruptures and presence of subparallel and branching fault traces, some earthquakes have more than two ends. Thus, in the case of the 1968 earthquake, it is accordingly depicted in Figure 14 that the fault ruptured through a 1.5-km restraining step, stopped on one end at either a 2.5-km restraining step or a 7-km releasing step, and stopped at the other end along an active trace that continues for 20 km or more in the absence of any observable discontinuity. Ruptures appear to have ended at the discontinuities depicted by large solid symbols, jumped across the discontinuities represented as large open squares and diamonds, and simply died out along strike in the absence of any discontinuities for the cases shown as gray circles. The observations show that about two-thirds of terminations of strike-slip ruptures are associated with geometrical steps in the fault trace or the termination of the active fault on which they occurred, that a transition exists between step dimensions of 3 and 4 km above which rupture fronts have not been observed to propagate through, and that ruptures appear to cease propagating at steps of lesser dimension only about 40% of the time (Fig. 15).

Earthquakes of Normal Mechanism. The approach followed for strike-slip events is applied to normal type earthquakes and summarized in Figures 16 and 17. The smaller data set makes it difficult to arrive at generalizations. That withstanding, the observations show that the end points of historical normal ruptures occur at discontinuities in the fault trace about 70% of the time. Historical normal fault ruptures have continued across steps in the surface trace of 5 to 7 km, larger than observed for the strike-slip earthquakes.

Earthquakes of Reverse Mechanism. The data for thrust faults are limited to eight earthquakes. Again ordered by increasing rupture length, I have plotted the discontinuities through which ruptures have propagated or stopped, respectively (Fig. 18). There are three recorded instances of thrust ruptures propagating through mapped steps of 2 and 6 km in dimension. In only one case is it clear that the rupture terminated in the absence of a discontinuity at the rupture end point. The remaining cases appear to show termini associated with geometrical discontinuities, though in several cases and particularly for the Australian earthquakes the mapping available is insufficient to lend any confidence in the observation.

Implications and Applications

Seismic Hazard

Estimation of Surface Rupture Hazard. The regression curves in Figure 7 provide an initial basis to estimate the expected amount of surface displacement during an earthquake as a function of rupture length. The values of slip plotted in Figure 7 are derived from the digitized slip distributions for the respective events as shown in Figure 1c. Each average value is also characterized by a standard deviation about the average. The COV (standard deviation/average slip) provides a measure of the roughness of the surface-slip distributions that is in effect normalized to rupture length. The value of the COV about the average value of slip for each event is displayed in Figure 10 (open circles). The average of all values is also listed in the plot and equals 0.63 ± 0.18. Given the expected rupture length of an earthquake, an average value of surface offset may be calculated from the regressions in Figure 7, and a standard deviation to associate with this latter estimate may, in principle, be calculated by multiplying the expected average slip by the COV.

The assessment of expected coseismic surface slip may be improved by assuming the surface slip is described by a particular shape such as the sine, ellipse, triangle, asymmetric sine, or asymmetric ellipse curve forms illustrated in Figure 9. Applying these curve forms consistently yields a better fit to the observed slip distributions than the average value of slip or, equivalently, a flat line (Fig. 10). One may thus choose an alternate approach of, for example, assuming that surface slip will follow the form of a sine or ellipse function. In doing so, the amplitude of expected distribution may be estimated as a function of length using the regression curves

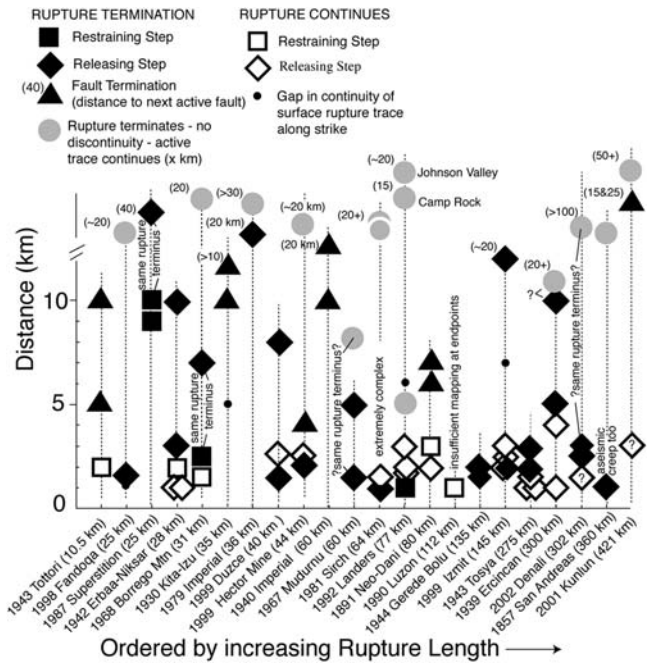

Figure 14. Synopsis of observations bearing on the relationship of geometrical discontinuities along the fault strike to the end points of historical strike-slip earthquake ruptures. Earthquake date, name, and rupture length are listed on the horizontal axis. The earthquakes are ordered by increasing rupture length (but are not scaled to the distance along the axis). Above the label of each earthquake is a vertical line, and symbols along the line represent the dimension of discontinuities within and at the end points of each rupture.

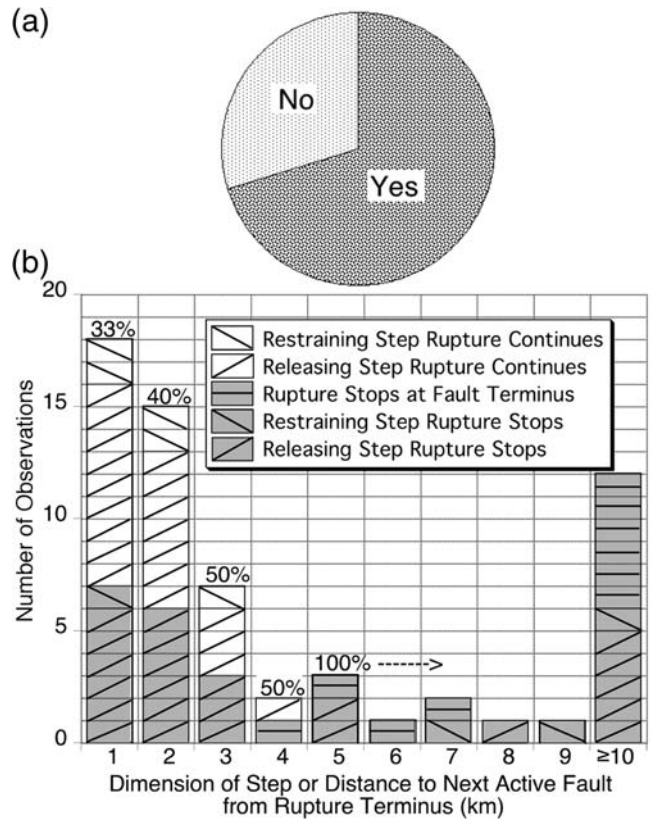

Figure 15. Relation of fault trace complexity to rupture length for strike-slip faults. (a) Pie chart of total number of rupture end points divided between whether (yes) or not (no) the end points are associated with a geometrical discontinuity (step or termination of rupture trace). About 70% of the time rupture end points are associated with such discontinuities. The remainder appear to simply die out along an active fault trace. The sample size is 46. (b) Histogram of the total number of geometrical discontinuities located along historical ruptures binned as a function of size ($\geq 1, \geq 2$, etc.) and shaded according to whether the particular step occurred at the end point of rupture or was broken through by the rupture. A transition occurs at 3–4 km above which no events have ruptured through and below which earthquakes have ruptured through in ~40% of the cases.

for the sine and ellipse functions in Figure 13d,e, respectively. Multiplication of the average value of the COV for the sine (0.57 ± 0.19) and ellipse (0.54 ± 0.19) curve fits by the predicted slip at any point along the fault length yields a standard deviation that may be attached to the estimate.

The earthquake slip distributions are yet better fit by the use of curves that allow an asymmetry in the slip distribution (Fig. 10), and further reduction in the uncertainties might be obtained by their use with the consideration that it would require prior knowledge of the sense of asymmetry along the fault to rupture. This is knowledge that is not generally available at this time.

A more formal approach than the one outlined here will incorporate both the uncertainties attendant to the fitting of curves to the slip versus length data (e.g., Figs. 7 and 13) and the estimates of the COVs (e.g., Figs. 9 and 10). That said, the compilation and analysis of observations show the feasibility of the approach, which is the main intent here.

Estimating the Length of Future Earthquake Ruptures on Mapped Faults. The distribution and lengths of active faults are generally fundamental inputs to assessments of seismic hazard in regions of active tectonics (e.g., Albee and Smith, 1966; Slemmons, 1977; Bonilla *et al.*, 1984; Wesnousky *et al.*, 1984; Wells and Coppersmith, 1994; WGCEP, 1995; Frankel and Petersen, 2002). Because the lengths of earthquake ruptures are commonly less than the entire length of the mapped fault on which they occur, the seismic hazard analyst may encounter the problem in deciding how to place limits on the probable lengths of future earthquakes on the mapped active faults. It has been noted previously that faults are not generally continuous but are commonly composed of segments that appear as steps in map view and that these discontinuities may play a controlling role in limiting the extent of earthquake ruptures (e.g., Segall and Pollard, 1980; Sibson, 1985; Wesnousky, 1988). The data collected here and summarized in Figure 14 show that about two-thirds of the end points of strike-slip earthquake ruptures are associated with fault steps or the termini of active fault traces (Fig. 15a), and that there is a limiting dimension of fault step (3–4 km) above which earthquake ruptures have not propagated and below which rupture propagations cease only about 40% of the time (Fig. 15b).

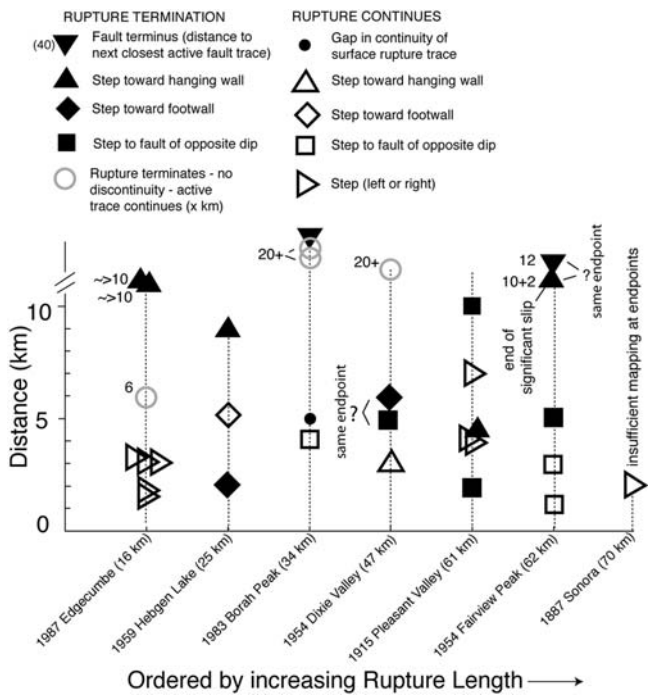

Figure 16. Synopsis of observations bearing on the relationship of geometrical discontinuities along the fault strike to the end points of normal mechanism historical earthquake ruptures. See Figure 14 for further explanation.

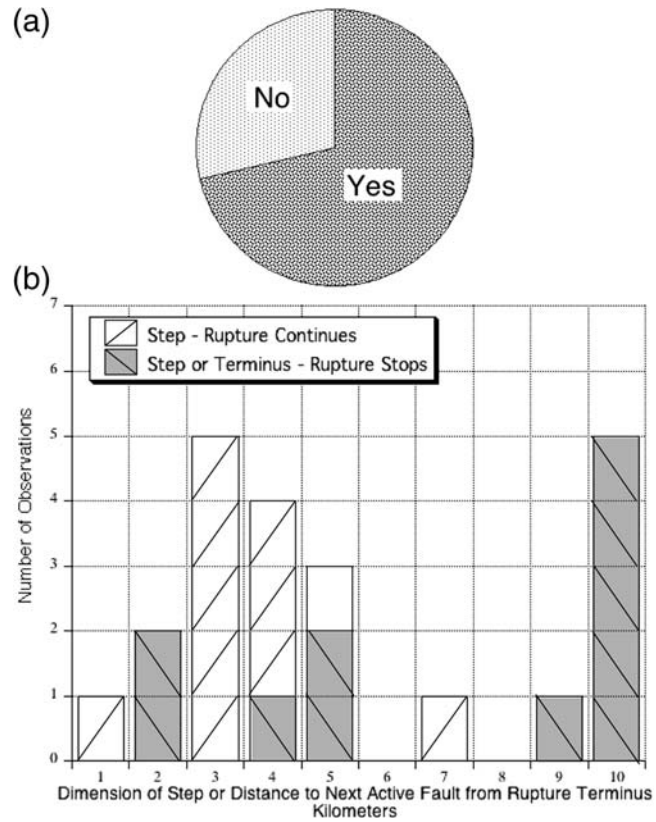

Figure 17. Relation of fault trace complexity to rupture length for normal faults. See Figure 15 for explanation. (a) About 75% of time rupture end points are associated with discontinuities in the fault trace. The remainder appear to end within an active fault trace in the absence of a discontinuity. The sample size is 14. (b) Normal fault ruptures cross steps in the fault strike as large as 5–7 km, larger than observed for strike-slip earthquakes.

The variability of behavior for steps of dimension less than 3–4 km in part reflects variability in the three-dimensional character of the discontinuities mapped at the surface. The effect on rupture propagation may vary between steps of equal map dimension if, for example, the subsurface structures differ or do not extend to equal depths through the seismogenic layer (e.g., Simpson *et al.*, 2006; Graymer *et al.*, 2007). The approach and observations might be useful for placing probabilistic bounds on the expected end points of future earthquake ruptures on mapped active faults, given that detailed mapping of faults is available in the region of interest.

The observations are fewer for dip-slip earthquakes (Figs. 16, 17, and 18). That withstanding, the normal earthquake rupture end points appear to be associated with discontinuities in the mapped fault trace at about the same ~70% frequency as observed for the strike-slip earthquakes (Fig. 17). The data are too few to draw an analogous generalization from the small number of reverse fault earthquakes. A comparison of the dip-slip (Fig. 16) to strike-slip earthquakes (Fig. 14) shows the dip-slip events to have ruptured through steps in map trace of 5–7 km, greater than observed for strike-slip earthquakes. The larger value may simply reflect the dipping nature of the faults.

Mechanics of the Rupture Process

Slip versus Length: Physical Implications. Theoretical models of fault displacements in an elastic medium predict that the stress drop $\Delta\sigma$ resulting from slip S on a fault is of the form $\Delta\sigma \cong C(S/W)$, where W is the shortest dimension across the fault area and C is a shape factor generally near unity (e.g., Kanamori and Anderson, 1975). Analyses of instrumental recordings of earthquakes have been the basis to interpret that stress drops for earthquakes are relatively constant and limited to between 10 and 100 bars over the entire spectrum of observed earthquake sizes (Kanamori and Anderson, 1975; Hanks, 1977). It is generally assumed that the limiting depth of coseismic slip is equal to the depth extent of aftershocks or background seismicity in the vicinity of the earthquakes. The earthquakes of Table 1 share a similar seismogenic depth of about 12–15 km (Fig. 2). It follows that earthquakes of constant stress drop and rupture width will share a similar ratio of S/W. The systematic increase in displacement S with rupture length observed in Figure 7 is thus in apparent conflict with the constant stress drop hypothesis, a point first recognized by Scholz (1982a). A number of observations and hypotheses have been brought forth to reconcile the issue.

Models of earthquake rupture conventionally impose the boundary condition that coseismic slip be mechanically limited to zero at the base of the seismogenic layer. The

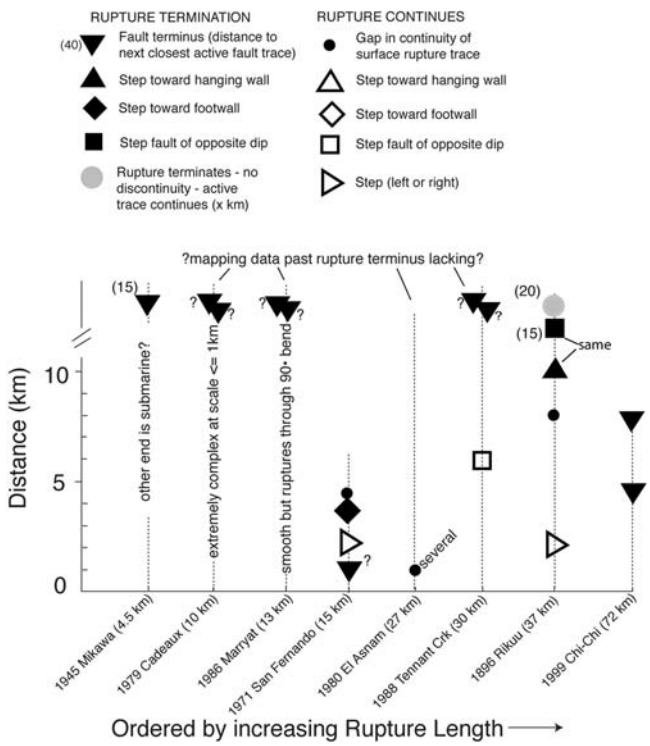

Figure 18. Synopsis of observations bearing on the relationship of geometrical discontinuities along the fault strike to the end points of thrust mechanism historical earthquake ruptures. Earthquake date, name, and rupture length are listed on the horizontal axis. The earthquakes are ordered by increasing rupture length (but not scaled to the distance along the axis). Above the label of each earthquake is a vertical line, and symbols along the line represent the dimension and type of discontinuities within and at the end points of each rupture.

observed increase in slip with length may be explained by modifying the boundary condition such that coseismic slip is a rapid upward extension of displacement that has accumulated below the seismogenic layer prior to the earthquake (Scholz, 1982a). Physical fault models arising from such an explanation predict that the time for displacement to occur at any point on a fault should be on the same order as the total duration of faulting (Scholz, 1982b). The idea is not supported by dislocation time histories of fault ruptures that are short compared to the overall duration of an earthquake (Heaton, 1990). Today, it appears to remain generally accepted that large earthquake ruptures are the result of simple elastic failure whereby displacements are limited to zero at the base of the seismogenic layer. Efforts to explain the enigmatic increase of S with L generally invoke the idea that large earthquakes commence with systematically larger stress drops or unusually large slip pulses relative to earthquakes of lesser size (Heaton, 1990; Bodin and Brune, 1996), and thus have a tendency to propagate over greater distances. Independent observations of the interaction of earthquake ruptures and the geometry of faults presented here and in Wesnousky (2006) are at odds with this latter idea. An alternate explanation is that the base of the seismogenic zone does not result from the onset of viscous relaxation but rather a transition to stable sliding in a medium that remains stressed at or close to failure and that coseismic slip during large earthquakes may extend below the seismogenic layer. The latter explanation is explored in more detail by King and Wesnousky (2007), satisfies standard elastic models, and preserves the idea of constant stress drop in light of the observed increase of S with L.

The Growth of Earthquake Ruptures. The majority of coseismic slip during continental earthquakes is generally concentrated in the upper 15 km of the earth's crust. The length of strike-slip ruptures considered here ranges from about 15 to >400 km. The direction of rupture propagation may be viewed as primarily horizontal for each event. Theoretical and numerical models and observation support the idea of a causal association between fault steps and the end points of earthquake ruptures (e.g., Segall and Pollard, 1980; Sibson, 1985; Wesnousky, 1988; Harris and Day, 1993; Harris and Day, 1999; Oglesby, 2005; Duan and Oglesby, 2006). The synopsis of observations in Figure 14 shows that there is a transition in step dimension at 3–4 km above which the strike-slip faults appear not to propagate and that the transition is largely independent of rupture length. The observation leads me to think that the magnitude of stress changes and the volume affected by those stress changes at the leading edge of propagating earthquake ruptures are similar at the initial stages of rupture propagation and largely invariable during the rupture process (Fig. 19). The transition of 3–4 km in step width above which ruptures have not propagated

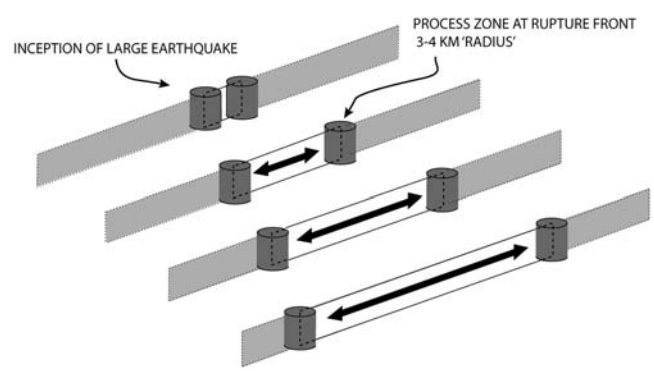

Figure 19. Schematic diagrams from the top left to the bottom right illustrate the increasing points in time of a rupture propagating bilaterally along a vertically dipping strike-slip fault plane. The unruptured and ruptured portion of the fault planes are shaded gray and white, respectively. Volumes around the rupture fronts capable of triggering slip on nearby fault segments are shaded dark gray. Empirical observations reviewed in this article of the interplay of the fault trace complexity and rupture propagation for large strike-slip earthquakes suggests a process whereby the magnitude of stress changes and volume affected by those stress changes at the front of a propagating rupture are largely the same and largely invariable during the rupture process, regardless of the distance a rupture has or will propagate.

by analogy places a limit on the dimension of process zone or volume significantly affected by stress changes at the rupture front. In this context, it appears that variations in earthquake rupture lengths are not necessarily controlled by the relative size of initial slip pulses or stress drops (e.g., Brune, 1968; Heaton, 1990) but rather by the geometrical complexity of fault traces (e.g., Wesnousky, 1988) and variations in accumulated stress levels along faults that arise due to the location of past earthquakes (e.g., McCann *et al.*, 1979).

The observations in Figure 12 that summarize the relationship between the location of earthquake epicenters and the asymmetry of slip distributions also have bearing on the topic of fault propagation. The observations show no systematic correlation between the initiation point of an earthquake and the location of maximum slip along the fault trace. The result is independent of which asymmetric curve fit is used to approximate the shape of the slip distributions and apparently at odds with observations indicating that earthquake epicenters of subduction zone thrust earthquakes tend to locate in or immediately adjacent to regions of high moment release (e.g., Thatcher, 1990). Indeed, while one may examine the figure and point to a number of earthquakes where the epicenter is spatially correlated to the peak of the slip distribution, there are numerous events where the epicenter is spatially separated from the peak. The latter observation is most evident for those events of unilateral rupture where the ratio E/L is close to 0 or 1. I view the observation to indicate that patterns of slip are not controlled by the relative size of initial slip pulses but likely instead by variations in accumulated stress reflecting variations in fault strength and accumulated stress along strike.

The Shape of Slip Distributions and Self-Similarity. The exercise of fitting curves to the slip distributions (Fig. 9) shows the unsurprising result that better fits to the observations are obtained with the increase in freely adjustable variables used in the regressions. The average (i.e., flat-line), symmetric (i.e., sine and ellipse), and asymmetric (i.e., asymmetric sine, asymmetric ellipse, and triangle) functions yield increasingly better fits to the observed slip distributions (Fig. 10). Similarly, the asymmetric forms may be viewed as a better approximation to the general shape of surface-slip distributions. The degree of asymmetry that one observes in fitting asymmetric functions to the slip distributions is dependent on the particular form of the function (Fig. 11). The assumption of a triangle function tends to exaggerate the asymmetry as compared to the asymmetric sine or ellipse. The exaggeration results because of the control of the assumed functions on the slope of the curve fit near the rupture end points. The scatter in values of asymmetry for the triangular and asymmetric ellipse curves would argue against the suggestion that the slip curves are self-similar in nature whereas the lessening of scatter in the value for the asymmetric sine fits might allow it (Fig. 11). The statistical differences in the triangle and asymmetric curve fits to the observations are insufficient to allow a resolution of the matter.

The systematic changes in slope attendant to the plots of the peak amplitudes of the curves fit to the surface-slip distributions versus rupture length shown in Figure 13 provide another manner in which to characterize the shapes of the surface-slip distributions. The plots show the same characteristics as observed in the earlier plots of average surface slip versus rupture length (Fig. 7). Specifically, the fewer normal and reverse earthquake data may be fit by a straight line but the strike-slip earthquakes that cover a wider range of rupture lengths cannot. The observations for the strike-slip earthquakes and the entire data set overall are better fit by curves that decrease with slope as a function of increasing rupture length. The suggestion has been put forth that earthquake slip distributions are self-similar in form (e.g., Manighetti *et al.*, 2005). The slope of the curves in Figures 7 and 13 reflects the ratio of amplitude to length of the assumed slip functions. In this regard, the ratios or, in effect, the shapes of the prescribed surface-slip distributions vary across the magnitude spectrum and may not be viewed as self-similar.

Conclusions

I have put forth a compilation of about three dozen historical earthquakes for which there exist both maps of earthquake rupture traces and data describing the coseismic surface slip observed along the fault strike. The analysis presented here may be of use in the development and application of seismic hazard methodologies and placing bounds on physical fault models meant to describe the earthquake source. In these regards, the collection of observations provide the basis for a statistical approach to predicting the end points and surface-slip distribution of earthquakes on mapped faults. They also lend support to the ideas that there exists a process zone at the edges of laterally propagating earthquake ruptures of no more than about 3–5 km in dimension within which stress changes may be sufficient to trigger slip on adjacent faults, and that the ultimate length of earthquake ruptures is controlled primarily by the geometrical complexity of fault traces and variations in accumulated stress levels along faults that arise due to the location of past earthquakes.

Acknowledgments

Thanks go to David Oglesby, Ivan Wong, and an anonymous reviewer for reviews of the manuscript, Senthil Kumar for assisting with the collection of maps, and Thorne Lay for clarifying the uncertainties attendant to the assumption of rigidity in the calculation of seismic moment. Support for the research was provided by the U.S. Geological Survey (USGS) National Earthquake Hazards Reduction Program (NEHRP) Award Number 07HQGR0108 and supplemented by the Southern California Earthquake Center (SCEC), which is funded by the National Science Foundation Cooperative Agreement Number EAR-0106924 and the USGS Cooperative Agreement Number 02HQAG0008. This paper is SCEC Contribution Number 1095 and the Center for Neotectonics Contribution Number 52.

References

Abe, K. (1978). Dislocations, source dimensions and stresses associated with earthquakes in the Izu Peninusula, Japan, *J. Phys. Earth* **26,** 253–274.

Aki, K., and P. G. Richards (1980). *Quantitative Seismology: Theory and Methods*, W. H. Freeman, New York, 932 pp.

Akyuz, H. S., R. Hartleb, A. Barka, E. Altunel, G. Sunal, B. Meyer, and R. Armijo (2002). Surface rupture and slip distribution of the 12 November 1999 Duzce Earthquake (*M* 7.1), North Anatolian Fault, Bolu, Turkey, *Bull. Seismol. Soc. Am.* **92,** no. 1, 61–66.

Albee, A. L., and J. L. Smith (1966). Earthquake characteristics and fault activity in southern California, in *Engineering Geology in Southern California*, R. Lung and R. Procter (Editors), Association of Engineering Geologists, Glendale, California, 9–33.

Allen, C. R., T. C. Hanks, and J. H. Whitcomb (1975). Seismological studies of the San Fernando earthquake and their tectonic implications, San Fernando, California, earthquake of 9 February 1971, *Calif. Div. Mines Geol. Bull. 196*, 257–262.

Allen, C. R., G. R. Engen, T. C. Hanks, J. M. Nordquist, and W. R. Thatcher (1971). Main shock and larger aftershocks of the San Fernando earthquake, February 9 through March 1, 1971, the San Fernando, California, earthquake of February 9, 1971, *U.S. Geol. Surv. Profess. Pap. 733*, 17–20.

Anderson, H., and T. Webb (1989). The rupture process of the 1987 Edgecumbe earthquake, New Zealand, *N. Z. J. Geol. Geophys.* **32,** 43–52.

Ando, M. (1974). Faulting in the Mikawa earthquake of 1945, *Tectonophysics* **22,** 173–186.

Antolik, M., R. E. Abercrombie, and G. Ekstrom (2004). The 14 November 2001 Kokoxili (Kunlunshan), Tibet, earthquake: rupture transfer through a large extensional step-over, *Bull. Seismol. Soc. Am.* **94,** no. 4, 1173–1194.

Barka, A. (1996). Slip distribution along the North Anatolian fault associated with the large earthquakes of the period 1939 to 1967, *Bull. Seismol. Soc. Am.* **86,** 1238–1254.

Barka, A., H. S. Akyuz, E. Altunel, G. Sunal, Z. Cakir, A. Dikbas, B. Yerli, R. Armijo, B. Meyer, J. B. de Chabalier, T. Rockwell, J. R. Dolan, R. Hartleb, T. Dawson, S. Christofferson, A. Tucker, T. Fumal, R. Langridge, H. Stenner, W. Lettis, J. Bachhuber, and W. Page (2002). The surface rupture and slip distribution of the 17 August 1999 Izmit Earthquake (*M* 7.4), North Anatolian fault, *Bull. Seismol. Soc. Am.* **92,** no. 1, 43–60..

Barrientos, S. E., R. S. Stein, and S. N. Ward (1987). Comparison of the 1959 Hebgen Lake, Montana and the 1983 Borah Peak, Idaho, earthquakes from geodetic observations, *Bull. Seismol. Soc. Am.* **77,** 784–808.

Beanland, S., K. R. Berryman, and G. H. Blick (1989). Geological investigations of the 1987 Edgecumbe earthquake, New Zealand, *N. Z. J. Geol. Geophys.* **32,** 73–91.

Ben-Menahem, A., and S. J. Singh (1981). *Seismic Waves and Sources* Springer-Verlag, New York, 1108 pp.

Ben-Zion, (2001). On quantification of the earthquake source, *Seism. Res. Lett.* **72,** no. 2, 1551–152.

Berberian, M., J. A. Jackson, E. J. Fielding, B. E. Parsons, K. F. Priestly, M. Qorashi, M. Talebian, R. Walker, T. J. Wright, and C. Baker (2001). The 1998 March 14 Fandoqa earthquake (M_w 6.6) in Kerman province, southeast Iran: re-rupture of the 1981 Sirch earthquake fault, triggering of slip on adjacent thrusts and the active tectonics of the Gowk fault zone, *Geophys. J. Int.* **146,** 371–398.

Bodin, P., and J. N. Brune (1996). On the scaling of slip with rupture length for shallow strike-slip earthquakes: quasi-static models and dynamic rupture propagation, *Bull. Seismol. Soc. Am.* **86,** 1292–1299.

Bonilla, M. G., R. K. Mark, and J. J. Leinkaemper (1984). Statistical relations among earthquake magnitude, surface rupture, and surface fault displacement, *Bull. Seismol. Soc. Am.* **74,** 2379–2411.

Brune, J. N. (1968). Seismic moment, seismicity, and rate of slip along major fault zones, *J. Geophys. Res.* **73,** 777–784.

Bull, W. B., and P. A. Pearthree (2002). Frequency and size of Quaternary surface ruptures of the Pitaycachi fault, northeastern Sonora, Mexico, *Bull. Seismol. Soc. Am.* **78,** 956–978.

Burdick, L., and G. R. Mellman (1976). Inversion of the body waves from the Borrego Mountain earthquake to source mechanism, *Bull. Seismol. Soc. Am.* **66,** 1485–1499.

Burgmann, R., M. E. Ayhan, E. J. Fielding, T. J. Wright, S. McClusky, B. Aktug, C. Demir, O. Lenk, and A. Turkezer (2002). Deformation during the 12 November 1999 Duzce, Turkey, earthquake, from GPS and InSAR data, *Bull. Seismol. Soc. Am.* **92,** 161–171.

Butler, R. (1983). Surface wave analysis of the 9 April 1968 Borrego mountain earthquake, *Bull. Seismol. Soc. Am.* **73,** 879–883.

Caskey, S. J., S. G. Wesnousky, P. Zhang, and D. B. Slemmons (1996). Surface faulting of the 1954 Fairview Peak ($M_s = 7.2$) and Dixie Valley ($M_s = 6.8$) earthquakes, central Nevada, *Bull. Seismol. Soc. Am.* **86,** 286–291.

Chi, W. C., D. Dreger, and A. Kaverina (2001). Finite-source modeling of the 1999 Taiwan (Chi-Chi) earthquake derived from a dense strong-motion network, *Bull. Seismol. Soc. Am.* **91,** 1144–1157.

Choy, G. L., and J. Boatwright (2004). Radiated energy and the rupture process of the Denali fault earthquake sequence of 2002 from broadband teleseismic body waves, *Bull. Seismol. Soc. Am.* **94,** 6B S269–S277.

Choy, G. L., and J. R. Bowman (1990). Rupture process of a multiple main shock sequence; analysis of teleseismic, local, and field observations of the Tennant Creek, Australia, earthquakes of Jan 22, 1988, *J. Geophys, Res,* **95,** 6867–6882.

Clark, M. M. (1972). Surface rupture along the Coyote Creek fault, the Borrego Mountain Earthquake of April 9, 1968, *U.S. Geol. Surv. Profess. Pap. 787*, 55–86.

Cohee, B. P., and G. C. Beroza (1994). Slip distribution of the 1992 Landers earthquake and its implications for earthquake source mechanics, *Bull. Seismol. Soc. Am.* **84,** 692–712.

Crone, A. J., M. N. Machette, and R. J. Bowman (1992). Geologic investigations of the 1988 Tennant Creek, Australia, earthquakes—implications for paleoseismicity in stable continental regions, *U.S. Geol. Surv. Bull.* **2032-A,** A1–A51.

Crone, A., M. Machette, D. Bonilla, J. Lienkamper, K. Pierce, W. Scott, and R. Bucknam (1987). Surface faulting accompanying the Borah Peak earthquake and segmentation of the Lost River Fault, central Idaho, *Bull. Seismol. Soc. Am.* **77,** 739–770.

Delouis, B., D. Giardini, P. Lundgren, and J. Salichon (2002). Joint inversion of InSAR, GPS, teleseismic, and strong-motion data for the spatial and temporal distribution of earthquake slip: application to the 1999 Izmit mainshock, *Bull. Seismol. Soc. Am.* **92,** 278–299.

Doser, D. I. (1985). Source parameters and faulting processes of the 1959 Hebgen Lake, Montana, earthquake sequence, *J. Geophys. Res.* **90,** 4537–4555.

Doser, D. I. (1986). Earthquake processes in the Rainbow Mountain–Fairview Peak–Dixie Valley, Nevada, region 1954–1959, *J. Geophys. Res.* **91,** 12,572–12,586.

Doser, D. I. (1988). Source parameters of earthquakes in the Nevada seismic zone, 1915–1943, *J. Geophys. Res.* **93,** 15,001–15,015.

Doser, D. I. (1990). Source characteristics of earthquakes along the southern San Jacinto and imperial fault zones (1937 to 1954), *Bull. Seismol. Soc. Am.* **80,** 1099–1117.

Doser, D. I., and H. Kanamori (1987). Long period surface waves of four western United States earthquakes recorded by the Pasadena strainmeter, *Bull. Seismol. Soc. Am.* **77,** 236–243.

Doser, D. I., and R. B. Smith (1985). Source parameters of the 28 October 1983 Borah Peak, Idaho, earthquake from body wave analysis, *Bull. Seismol. Soc. Am.* **75,** 1041–1051.

Dreger, D. (1994). Investigation of the rupture process of the 28 June 1992 Landers earthquake utilizing TERRAscope, *Bull. Seismol. Soc. Am.* **84,** 713–724.

Duan, B., and D. D. Oglesby (2006). Heterogeneous fault stresses from previous earthquakes and the effect on dynamics of parallel strike-slip faults, *J. Geophys. Res.* **111,** B05309, doi 10.1029/2005JB004138.

Dziewonki, A. M., G. Ekstrom, J. H. Woodhouse, and G. Zwart (1989). Centroid-moment tensor solutions for October–December 1987, *Phys. Earth Planet. Inter.* **54,** 10–21.

Ebel, J. E., and D. V. Helmberger (1982). *P*-wave complexity and fault asperities: the Borrego Mountain, California, earthquake of 1968, *Bull. Seismol. Soc. Am.* **72,** 413–437.

Eberhart-Phillips, D., P. J. Haeussler, J. T. Freymueller, A. D. Franckel, C. M. Rubin, P. Craw, N. A. Ratchkovski, G. Anderson, G. A. Carver, A. J. Crone, T. E. Dawsson, H. Fletcher, R. Hansen, E. L. Harp, R. A. Harris, D. P. Hill, S. Hreinsdottiir, R. W. Jibson, L. M. Jones, R. Kayen, D. K. Keefer, C. F. Larsen, S. C. Moran, S. F. Personius, G. Plafker, B. Sherrod, K. Sieh, N. Sitar, and W. K. Wallace (2003). The 2002 Denali fault earthquake, Alaska: a large magnitude, slip-partitioned event, *Science* **300,** 1113–1118.

Frankel, A. (2004). Rupture process of the *M* 7.9 Denali fault, Alaska, earthquake: subevents, directivity, and scaling of high-frequency ground motions, *Bull. Seismol. Soc. Am.* **94,** no. 6B, S234–S255.

Frankel, A. D., and M. D. Petersen (2002). Documentation for the 2002 update of the national seismic hazard maps, *U.S. Geol. Surv. Open-File Rept. 02-0420*, 33 pp.

Frankel, A., and L. Wennerberg (1989). Rupture process of the M_s 6.6 Superstition Hills earthquake determined from strong-motion recordings: application of tomographic source inversion, *Bull. Seismol. Soc. Am.* **79,** 515–541.

Fredrich, J., R. McCaffrey, and D. Denham (1988). Source parameters of seven large Australian earthquakes determined by body waveform inversion, *Geophys. J. R. Astron. Soc.* **95,** 1–13.

Freymueller, J. (1994). The co-seismic slip distribution of the Landers earthquake, *Bull. Seismol. Soc. Am.* **84,** 646–659.

Fuis, G. S., and L. A. Wald (2003). Rupture in south-central Alaska—the Denali fault earthquake of 2002, *U.S. Geol. Surv. Fact Sheet 014-03 (March)*, 4 pp.

Graymer, R. W., V. E. Langenheim, R. W. Simpson, R. C. Jachens, and D. A. Ponce (2007). Relatively simple through-going fault planes at large-earthquake depth may be concealed by the surface complexity of strike-slip faults, in Bends, Sedimentary Basins and Earthquake Hazards, in *Tectonics of Strike-Slip Restraining and Releasing Bends*, Geological Society, London, Special Publications, Vol. **290**, 189–201.

Haeussler, P. J., D. P. Schwartz, T. Dawson, H. Stenner, J. L. Lienkaemper, B. Sherrod, F. R. Cinti, and P. Montone (2005). Surface rupture and slip distribution of the Denali and Totschunda faults in the 3 November 2002 *M* 7.9 earthquake, Alaska, *Bull. Seismol. Soc. Am.* **94,** no. 6B, S23–252.

Hanks, T. C. (1977). Earthquake stress drops, ambient tectonic stresses and stresses that drive plate motion, *Pure Appl. Geophys.* **115,** 441–458.

Hanks, T. C., and M. Wyss (1972). The use of body-wave spectra in determination of seismic-source parameters, *Bull. Seismol. Soc. Am.* **62,** 561–589.

Harris, R. A., and S. M. Day (1993). Dynamics of fault interaction—parallel strike-slip faults, *J. Geophys. Res.* **18,** 4461–4472.

Harris, R. A., and S. M. Day (1999). Dynamic 3D simulations of earthquakes on en echelon faults, *Geophys. Res. Lett.* **98,** 2089–2092.

Hartzell, S. H., and T. Heaton (1983). Inversion of strong ground-motion and teleseismic waveform data for the fault rupture history of the 1979 Imperial Valley, California, earthquake sequence, *Bull. Seismol. Soc. Am.* **73,** 1553–1584.

Hartzell, S. H., and D. V. Helmberger (1982). Strong-motion modeling of the Imperial Valley earthquake of 1979, *Bull. Seismol. Soc. Am.* **72,** 571–596.

Heaton, T. H. (1982). The 1971 San Fernando earthquake: a double event?, *Bull. Seismol. Soc. Am.* **72,** 2037–2062.

Heaton, T. H. (1990). Evidence for and implication of self-healing pulses of slip in earthquake rupture, *Phys. Earth Planet. Inter.* **64,** 1–20.

Heaton, T., and D. V. Helmberger (1977). A study of the strong ground motion of the Borrego Mountain, California earthquake, *Bull. Seismol. Soc. Am.* **67,** 315–330.

Hodgkinson, K. M., R. S. Stein, and G. Marshall (1996). Geometry of the 1954 Fairview Peak–Dixie Valley earthquake sequence from a joint inversion of leveling and triangulation data, *J. Geophys. Res.* **101,** 25,437–25,457.

Hwang, L. J., H. Magistrale, and H. Kanamori (1990). Teleseismic source parameters and rupture characteristics of the 24 November 1987, Superstition Hills earthquake, *Bull. Seismol. Soc. Am.* **80,** 43–56.

Ji, C., D. J. Wald, and D. V. Helmberger (2002). Source description of the 1999 Hector Mine, California, earthquake, part I: wavelet domain inversion theory and resolution analysis, *Bull. Seismol. Soc. Am.* **92,** no. 4, 192–1207.

Johnson, C. E., and L. K. Hutton (1982). Aftershocks and preearthquake seismicity in the Imperial Valley California, earthquake of October 15, 1979, *U.S. Geol. Surv. Profess. Pap., 1254*, 59–76.

Johnson, H. O., D. C. Agnew, and K. Hudnut (1994). Extremal bounds on earthquake movement from geodetic data-application to the Landers earthquake, *Bull. Seismol. Soc. Am.* **84,** 660–667.

Jonsson, S., H. Zebker, P. Segall, Amelung, and F. (2002). Fault slip distribution of the 1999 M_w 7.1 Hector Mine, California earthquake, estimated from satellite radar and GPS measurements, *Bull. Seismol. Soc. Am.* **92,** 4, 1377–1389.

Kakehi, Y., and T. Iwata (1992). Rupture process of the 1945 Mikawa earthquake as determined from strong ground motion records, *J. Phys. Earth* **40,** 635–655.

Kanamori, H. (1973). Mode of strain release associated with major earthquakes in Japan, *Ann. Rev. Earth Planet. Sci.* **1,** 213–239.

Kanamori, H., and D. Anderson (1975). Theoretical basis of some empirical relations in seismology, *Bull. Seismol. Soc. Am.* **65,** 1073–1096.

Kanamori, H., and J. Reagan (1982). Long-period surface waves, *U.S. Geol. Surv. Profess. Pap., 1254*, 55–58.

Kaneda, H., and A. Okada (2002). Surface rupture associated with the 1943 Tottori earthquake: compilation of previous reports and its tectonic geomorphological implications, *Active Fault Res.* **21,** 73–91 (in Japanese with English abstract).

Kaverina, A., D. Dreger, and E. Price (2002). The combined inversion of seismic and geodetic data for the source process of the 16 October 1999 M_w 7.1 Hector Mine, earthquake, *Bull. Seismol. Soc. Am.* **92,** no. 4, 1266–1280.

Kikuchi, M., M. Nakamura, and K. Yoshikawa (2003). Source rupture processes of the 1944 Tonankai earthquake and the 1945 Mikawa earthquake derived from low-gain seismograms, *Earth Planet. Space* **55,** 159–172.

King, G. C. P., and S. G. Wesnousky (2007). Scaling of fault parameters for continental strike-slip earthquakes, *Bull. Seismol. Soc. Am.* **97,** no. 6, 1833–1840.

Klinger, Y., R. Michel, and G. C. P. King (2006). Evidence for an earthquake barrier model from $M_w \sim 7.8$ Kokozili (Tibet) earthquake slip distribution, *Earth Planet. Sci. Lett.* **242,** 354–364.

Klinger, Y., X. Xu, P. Tapponier, J. Van der Woerd, C. Lasserre, and G. C. P. King (2005). High-resolution satellite imagery mapping of the surface rupture and slip distribution of the $M_w \sim 7.8$, 14 November 2001 Kokoxili earthquake, Kunlun fault, northern Tibet, China, *Bull. Seismol. Soc. Am.* **95,** 1970–1987.

Kramer, S. L. (1996). *Geotechnical Earthquake Engineering*, Prentice Hall, New York, 653 pp.

Langston, C. A. (1978). The February 9, 1971 San Fernando earthquake: a study of source finiteness in teleseismic body waves, *Bull. Seismol. Soc. Am.* **68,** 1–29.

Langston, C. A. (1987). Depth of faulting during the 1968 Meckering, Australia, earthquake sequence determined from wave form analysis of local seismograms, *J. Geophys. Res.* **92,** 11,561–11,574.

Larsen, S., R. Reilinger, H. Neugebauer, and W. Strange (1992). Global positioning system measurements of deformations associated with

the 1987 Superstition Hills earthquake, *J. Geophys. Res.* **97,** 4885–4902.

Lasserre, C., G. Peltzer, F. Crampé, Y. Klinger, J. Van der Woerd, and P. Tapponnier (2005). Coseismic deformation of the 2001 $M_w = 7.8$ Kokoxili earthquake in Tibet, measured by synthetic aperture radar interferometry, *J. Geophys. Res.* **110,** B12408, doi 10.1029/2004JB003500.

Lewis, J. D., N. A. Daetwyler, J. A. Bunting, and J. S. Moncrieff (1981). Report 11, The Cadeaux earthquake, 2 June 1979, Geological Survey of Western Australia, 134 pp.

Li, X., V. Cormier, and M. N. Toksoz (2002). Complex source process of the 17 August 1999 Izmit, Turkey, earthquake, *Bull. Seismol. Soc. Am.* **92,** 267–277.

Lin, A., T. Ouchi, A. Chen, and T. Maruyama (2001). Co-seismic displacements, folding and shortening structures along the Chelungpu surface rupture zone occurred during the 1999 Chi-Chi (Taiwan) earthquake, *Tectonophysics* **330,** 225–244.

Lin, A., F. Bihong, J. Guo, Q. Zeng, G. Dang, W. He, and Y. Zhao (2002). Co-seismic strike-slip and rupture length produced by the 2001 M_s 8.1 central Kunlun earthquake, *Science* **296,** 2015–2017.

Machette, M. N., A. J. Crone, and J. R. Bowman (1993). Geologic investigations of the 1986 Marryat Creek, Australia, earthquake—implications for paleoseismicity in stable continental regions, *U.S. Geol. Surv. Bull.* **2032,** no. B, 29 pp.

Manighetti, I., M. Campillo, C. Sammis, P. M. Mai, and G. King (2005). Evidence for self-similar, triangular slip distributions on earthquakes: implications for earthquake fault mechanics, *J. Geophys. Res.* **110,** B05302, doi 10.1029/2004JB003174.

Matsuda, T. (1972). Surface faults associated with Kita-Izu earthquake of 1930 in Izu Peninsula, Japan, in *Izu Peninsula*, M. Hoshino and H. Aoki (Editors), Tokai University Press, Tokyo, 73–102.

Matsuda, T. (1974). Surface faults associated with Nobi (Mino-Owari) Earthquake of 1891, Japan, *Bull. Earthq. Res. Inst., Univ. Tokyo* **13,** 127–162.

Matsuda, T., H. Yamazaki, T. Nakata, and T. Imaizumi (1980). The surface faults associated with the Rikuu Earthquake of 1896, *Bull. Earthq. Res. Inst., Univ. Tokyo* **55,** 795–855.

McCann, W. R., S. P. Nishenko, L. R. Sykes, and J. Krause (1979). Seismic gaps and plate tectonics: seismic potential for major boundaries, *Pure Appl. Geophys.* **117,** 1082–1147.

Mendoza, C., and S. H. Hartzell (1988). Inversion for slip distribution using teleseismic *P* waveforms: North Palm Springs, Borah Peak, and Michoacan earthquakes, *Bull. Seismol. Soc. Am.* **78,** 1092–1111.

Nakata, T. (1990). Surface faulting associated with the Philippine earthquake of 1990, *J. Geogr.* **99,** no. 5, 95–112 (in Japanese).

Oglesby, D. D. (2005). The dynamics of strike-slip step-overs with linking dip-slip faults, *Bull. Seismol. Soc. Am.* **95,** 1604–1622.

Ozacar, A. A., and S. L. Beck (2004). The 2002 Denali fault and 2001 Kunlun fault earthquakes: complex rupture processes of two large strike-slip events, *Bull. Seismol. Soc. Am.* **94,** no. 6, S278–S292.

Petersen, M. D., and S. G. Wesnousky (1994). Fault slip rates and earthquake histories for active faults in southern California, *Bull. Seismol. Soc. Am.* **84,** 1608–1649.

Pezzopane, S. K., and T. E. Dawson (1996). Fault displacement hazard: a summary of issues and information, in *Seismotectonic Framework and Characterization of Faulting at Yucca Mountain*, Whitney, J. W. (Editor), Department of Energy, Las Vegas, 9-1–9-160.

Pinar, A., Y. Hohkura, and M. Kikuchi (1996). A rupture model for the 1967 Mudurnu Valley, Turkey earthquake and its implication for seismotectonics in the western part of the North Anatolian fault zone, *Geophys. Res. Lett.* **23,** 29–32.

Press, W. H., S. A. Teukolsky, W. T. Vetterliing, and B. P. Flannnery (1992). Numerical recipes in Fortran: an art of scientific computing, Cambridge University Press, New York, 963 pp.

Priestly, K. F. (1987). Source parameters of the 1987 Edgecumbe earthquake, New Zealand, *N. Z. J. Geol. Geophys.* **32,** 53–59.

Reilinger, R. (1984). Coseismic and postseismic vertical movements associated with the 1940 *M* 7.1 Imperial Valley, California, earthquake, *J. Geophys. Res.* **89,** 4531–4538.

Romanowicz, B. (1994). Comment on "A reappraisal of large earthquake scaling", *Bull. Seismol. Soc. Am.* **84,** 1675–1676.

Rowland, J. V., and R. H. Sibson (2004). Structural controls on hydrothermal flow in a segmented rift system, Taupo Volcanic Zone, New Zealand, *Geofluids* **4,** 259–283.

Scholz, C. (1982a). Scaling laws for large earthquakes: consequences for physical models, *Bull. Seismol. Soc. Am.* **72,** 1–14.

Scholz, C. (1982b). Scaling relations for strong ground motion in large earthquakes, *Bull. Seismol. Soc. Am.* **72,** 1903–1909.

Scholz, C. H. (1994). Reply to "Comment on 'A reappraisal of large earthquake scaling' by C Scholz", *Bull. Seismol. Soc. Am.* **84,** 1677–1678.

Segall, P., and D. D. Pollard (1980). Mechanics of discontinuous faults, *J. Geophys. Res.* **85,** 4337–4350.

Sekiguchi, H., and T. Iwata (2002). Rupture process of the 199 Kocaeli, Turkey, earthquake estimated from strong motion waveforms, *Bull. Seismol. Soc. Am.* **92,** 300–311.

Sharp, R., J. Lienkamper, D. Bonilla, D. Burke, B. Fox, D. Herd, D. Miller, D. Morton, D. Ponti, J. Rymer, J. Tinsley, and J. Yount (1982). Surface faulting in the Central Imperial Valley in the Imperial Valley California, earthquake of October 15, 1979, *U.S. Geol. Surv. Profess. Pap., 1254*.

Sharp, R., K. Budding, J. Boatwright, M. Ader, M. Bonilla, M. Clark, T. Fumal, T. Harms, J. Lienkaemper, D. Morton, B. O'Neill, C. Ostergren, D. Ponti, M. Rymer, J. Saxton, and J. Sims (1989). Surface faulting along the Superstition Hills fault zone and nearby faults associated with the earthquakes of 24 November 1987, *Bull. Seismol. Soc. Am.* **79,** 252–281.

Sibson, R. H. (1985). Stopping of earthquake ruptures at dilational fault jogs *Nature* **316,** no. 6025, 248–251.

Sieh, K. E. (1978). Slip along the San Andreas fault associated with the great 1857 earthquake, *Bull. Seismol. Soc. Am.* **68,** 1421–1448.

Sieh, K., L. Jones, E. Hauksson, K. Hudnut, P. Eberhart, T. Heaton, T. Hough, L. Hutton, H. Kanamori, A. Lilje, S. Lindvall, S. McGill, J. Mori, C. Rubin, J. Spotila, J. Stock, H. Thio, J. Treiman, B. Wernicke, and J. Zachariasen (1993). Near-field investigations of the Landers earthquake sequence, April to July 1992, *Science* **260,** 171–176.

Simpson, R. W., M. Barall, J. Langbein, J. R. Murray, and M. J. Rymer (2006). San Andreas fault geometry in the Parkfield, California, region, *Bull. Seismol. Soc. Am.* **96,** no. 4B, S28–S37.

Sipkin, S. A. (1989). Moment-tensor solutions for the 24 November 1987 Superstition Hills, California earthquake, *Bull. Seismol. Soc. Am.* **79,** 493–499.

Slemmons, D. B. (1977). State of the art for assessing earthquake hazards in the United States: determination of the design earthquake magnitude from fault length and maximum displacement data, U.S. Army Eng. Waterways Exp. Station, Vicksburg, Mississippi.

Stewart, G. S., and H. Kanamori (1982). Complexity of rupture in large strike-slip earthquakes in Turkey, *Phys. Earth Planet. Inter.* **28,** 70–84.

Suter, M., and J. Contreras (2002). Active tectonics of northeastern Sonora, Mexico (southern Basin and Range Province) and the 3 May 1887 M_w 7.4 earthquake, *Bull. Seismol. Soc. Am.* **92,** 581–589.

Swanger, H. J., and D. M. Boore (1978). Simulation of strong-motion displacements using surface-wave modal superposition, *Bull. Seismol. Soc. Am.* **68,** 907–922.

Tanimoto, T., and H. Kanamori (1986). Linear programming approach to moment tensor inversion of earthquake sources and some tests on the three-dimensional structure of the upper mantle, *Geophys. J. R. Astron. Soc.* **84,** 413–430.

Taymaz, T., J. A. Jackson, and D. McKenzie (1991). Active tectonics of the north and central Aegean Sea, *Geophys. J. Int.* **108,** 589–603.

Thatcher, W. (1990). Order and diversity in the modes of Circum–Pacific earthquake recurrence, *J. Geophys. Res.* **95,** 2609–2623.

Thatcher, W., and T. C. Hanks (1973). Source parameters of southern California earthquakes, *J. Geophys. Res.* **78,** 8547–8576.

Treiman, J., K. J. Kendrick, W. A. Bryant, T. K. Rockwell, and S. F. McGill (2002). Primary surface rupture associated with the M_w 7.1 16 October 1999 Hector Mine earthquake, San Bernardino County, California, *Bull. Seismol. Soc. Am.* **92,** no. 4, 1171–1191.

Trifunac, M. D. (1972). Tectonic stress and the source mechanism of the Imperial Valley, California, earthquake of 1940, *Bull. Seismol. Soc. Am.* **62,** 1283–1302.

Trifunac, M. D., and J. Brune (1970). Complexity of energy release during the Imperial Valley, California, earthquake of 1940, *Bull. Seismol. Soc. Am.* **60,** 137–160.

Tsuya, K. (1946). The Fukozu fault. A remarkable earthquake fault formed during the Mikawa earthquake of January 13, 1945, *Bull. Earthq. Res. Inst., Tokyo Univ.* **24,** 59–76 (in Japanese with English abstract).

Umutlu, N., K. Koketsu, and C. Milkereit (2004). The rupture process during the 1999 Duzce, Turkey, earthquake from joint inversion of teleseismic and strong-motion data, *Tectonophysics* **391,** 315–324.

Velasco, A. A., J. J. Ammon, T. Lay, and M. Hagerty (1996). Rupture process of the 1990 Luzon, Phillippines ($M_w = 7.7$) earthquake, *J. Geophys. Res.* **101,** 22,419–22,434.

Vidale, J., D. V. Helmberger, and R. W. Clayton (1985). Finite difference seismograms for *SH* waves, *Bull. Seismol. Soc. Am.* **75,** 1765–1782.

Wald, D. J., and T. Heaton (1994). Spatial and temporal distribution of slip for the 1992 Landers, California, earthquake, *Bull. Seismol. Soc. Am.* **84,** 668–691.

Wald, D. J., D. V Helmberger, and S. H. Hartzell (1990). Rupture process of the 1987 Superstition Hills earthquake from the inversion of strong-motion data, *Bull. Seismol. Soc. Am.* **80,** 1079–1098.

Wallace, R. E. (1980). Map of fault scarps formed during earthquake of October 2, 1915, Pleasant Valley, Nevada, and other young fault scarps, *U.S. Geol. Surv, Open-File Rept, 80-0608*.

Ward, S. N., and S. E. Barrientos (1986). An inversion for slip distribution and fault shape from geodetic observations of the 1983 Borah Peak, Idaho, earthquake, *J. Geophys. Res.* **91,** 4909–4919.

Wells, D. L., and K. J. Coppersmith (1994). New empirical relationships among magnitude rupture length, rupture width, rupture area, and surface displacement, *Bull. Seismol. Soc. Am.* **75,** 939–964.

Wesnousky, S. (1988). Seismological and structural evolution of strike-slip faults, *Nature* **335,** no. 6188, 340–342.

Wesnousky, S. G. (1986). Earthquakes, Quaternary faults, and seismic hazard in California, *J. Geophys. Res.* **91,** 12,587–12,631.

Wesnousky, S. G. (2006). Predicting the endpoints of earthquake ruptures, *Nature* **444,** no. 16, 358–360.

Wesnousky, S. G., C. H. Scholz, K. Shimazaki, and T. Matsuda (1984). Integration of geological and seismological data for the analysis of seismic hazard: a case study of Japan, *Bull. Seismol. Soc. Am.* **74,** 687–708.

Witkind, I. J. (1964). Reactivated faults north of Hebgen Lake, *U.S. Geol. Surv. Profess. Pap., 435-G*, 37–50.

Working Group on California Earthquake Probabilities (WGCEP) (1995). Seismic hazards in southern California: probable earthquakes, 1994–2024, *Bull. Seismol. Soc. Am.* **85,** 379–439.

Wu, C. J., M. Takeo, and S. Ide (2001). Source process of the Chi-Chi earthquake: a joint inversion of strong motion data and global positioning system data with multifault model, *Bull. Seismol. Soc. Am.* **91,** 1128–1143.

Wyss, M. (1971). Preliminary source parameter determination of the San Fernando earthquake, the San Fernando, California, earthquake of February 9, 1971, U.S. Government Printing Office, Washington, D.C., 38–40.

Xu, X., W. Chen, W. Ma, G. Yu, and G. Chen (2002). Surface rupture of the Kunlunshan earthquake (M_s 8.1), northern Tibetan plateau, China, *Seism. Res. Lett.* **73,** no. 6, 884–892.

Yielding, G., J. A. Jackson, G. C. P. King, H. Sinvhal, C. Vita-Finzi, and R. M. Wood (1981). Relations between surface deformation, fault geometry, seismicity, and rupture characteristics during the El Asnam (Algeria) earthquake of 10 October 1980, *Earth Planet. Sci. Lett.* **56,** 287–304.

Yomogida, K., and T. Nakata (1994). Large slip velocity of the surface ruptures associated with the 1990 Luzon earthquake, *Geophys. Res. Lett.* **21,** 1799–1802.

Yoshida, Y., Abe, and K. (1992). Source mechanism of the Luzon, Philippines earthquake of July 16, 1990, *Geophys. Res. Lett.* **19,** 545–548.

Zeng, Y., Chen, and C. H. (2001). Fault rupture process of the 20 September 1999 Chi-Chi, Taiwan earthquake, *Bull. Seismol. Soc. Am.* **91,** 1088–1098.

Center for Neotectonic Studies
Mail Stop 169
University of Nevada
Reno, Nevada 89557
stevew@seismo.unr.edu

Manuscript received 1 May 2007